

Facile preparation of Bi-doped ZnO/ β -Bi₂O₃/Carbon xerogel composites towards visible-light photocatalytic applications: Effect of calcination temperature and bismuth content



Nicolas Perciani de Moraes^a, Robson da Silva Rocha^a, Maria Lucia Caetano Pinto da Silva^a, Tiago Moreira Bastos Campos^b, Gilmar Patrocínio Thim^b, Richard Landers^c, Liana Alvares Rodrigues^{a,*}

^a Escola de Engenharia de Lorena-EEL/USP, Estrada Municipal do Campinho S/N, CEP 12602-810, Lorena, São Paulo, Brazil

^b Instituto Tecnológico de Aeronáutica-ITA/CTA, Praça Mal. Eduardo Gomes 50, CEP 12228-900, São José dos Campos, São Paulo, Brazil

^c Universidade de Campinas, Instituto de Física “Gleb Wataghin”, 500, Avenida Albert Einstein, CEP: 13083-852, Campinas, SP, Brazil

ARTICLE INFO

Keywords:

Zinc oxide
Bismuth oxide
Photocatalysis
Heterojunction
Carbon xerogel

ABSTRACT

This work aimed to study the development and properties of Bi-doped ZnO/ β -Bi₂O₃/Carbon xerogel composites towards visible light photocatalysis applications. The materials were characterized by X-ray diffraction, scanning electron microscopy, transmission electron microscopy, dispersive energy spectroscopy, infrared spectroscopy, nitrogen adsorption isotherms, Raman spectroscopy, diffuse reflectance spectroscopy and X-ray photoelectron spectroscopy. The photocatalytic activity of the developed composites was evaluated through the photodegradation of the 4-chlorophenol molecule and by chronoamperometry tests. The results obtained show that the calcination temperature poses a major influence in the final structure of the materials developed. The calcination temperature of 600 °C resulted in the formation of the β -Bi₂O₃ and Bi⁰ phases, consequently enhancing the photocatalytic activity of the composites due to the increased charge mobility provided by the heterojunctions between zinc oxide, carbon xerogel, bismuth oxide and metallic bismuth. The composite with intermediate bismuth composition (XC/ZnO–Bi₂O₃ 5%) displayed the best photocatalytic response among the materials tested, which was confirmed by its increased photocurrent generation capability. The photocatalytic mechanism is highly dependent in the generation of hydroxyl radicals and the composite presents good reusability properties.

1. Introduction

Currently, the study of clean and efficient technologies for the remediation of industrial environmental pollution has attracted significant attention from the scientific community, mainly due to the increase in global awareness regarding environmental conservation and the increased importance of sustainable industrial processes [1]. Heterogeneous photocatalysis has been shown to be a particularly suitable process for the decontamination of wastewaters containing organic compounds with high toxicity and low biodegradability. This process is advantageous due to its ability to promote complete mineralization of toxic molecules, contrary to conventional adsorption and flocculation processes, which are based on the transfer of such species onto another phase [2].

The fundamental principle of the photocatalytic phenomenon is the

photoactivation of a semiconductor by light. This interaction causes electrons in the valence band (VB) to migrate to the conduction band (CB), generating vacancies in the VB and photoexcited electrons in the CB. This process is responsible for the generation of free radicals in aqueous medium, such as hydroxyl and superoxide, which will be responsible for the oxidation of organic pollutants. However, these radicals will not be available for the redox reaction if the electron-vacancy pair recombines, which leads to a drastic reduction in the photodegradation efficiency of the process [3].

Among the most used photocatalysts, zinc oxide (ZnO) is widely applied in photocatalytic processes under ultraviolet radiation due to its suitable bandgap energy (≈ 3.3 eV). This use of this material in such applications is advantageous due to its ubiquity, negligible toxicity, elevated electronic mobility and facile synthesis [4]. However, ZnO has fast recombination of photogenerated charges, and its absorption of

* Corresponding author.

E-mail address: liana.r@usp.br (L.A. Rodrigues).

<https://doi.org/10.1016/j.ceramint.2020.06.166>

Received 16 April 2020; Received in revised form 20 May 2020; Accepted 15 June 2020

Available online 27 June 2020

0272-8842/ © 2020 Elsevier Ltd and Techna Group S.r.l. All rights reserved.

radiation in the visible region is limited, which makes its use impracticable in processes based on natural light [5]. In this context, modifications must be studied in order to suppress the recombination of photogenerated charges and increase the semiconductor's sensitivity to visible radiation.

An efficient way to enhance the photoactivity of a photocatalyst is the p-n semiconductor heterojunction. In general, when semiconductors of types n and p are in contact, an electrically charged region is formed in the heterojunction between the materials, due to the charge transfer between the semiconductors. When these semiconductors are irradiated with photons of energy greater than their bandgap energy, the photo-generated charges are easily separated due to the electric field present in the heterojunction between the semiconductors. Due to this phenomenon, electrons are transferred to the conduction band of the n-type semiconductor and vacancies are transferred to the valence band of the p-type semiconductor. Thus, a decrease in electron-vacancy pair recombination is achieved, increasing the photocatalytic activity of the developed material [6,7]. In this context, Wang et al. [8] produced ZnO/ α -Bi₂O₃ heterojunctions by solid state reaction, demonstrating that the material composed by the junction of the two oxides is superior in the discoloration of dyes under solar radiation, when compared to pure oxides. This result was explained by the enhanced charge separation obtained during the photocatalytic process. Similar results were obtained by Medina et al. [9], that verified the superiority of the ZnO/ α -Bi₂O₃ composite in the degradation of the indigo carmine dye under visible radiation.

Doping with metallic bismuth (Bi⁰) can also be seen as a promising modification for the optimization of the photocatalytic efficiency, as the heterojunction between metal and semiconductor leads to the formation of the so-called Schottky barrier. This barrier consists of a charged region in the heterojunction between semiconductor and metal, so that at the interface between materials electrons flow from the material with the highest Fermi energy (semiconductor) to the material with the lowest Fermi energy (metal). Thus, the photogenerated electrons are transferred from the semiconductor to the metallic phase, inhibiting the recombination of the electron-vacancy pair [6]. The literature related to the phenomenon reports the increased efficiency of both zinc oxide and bismuth oxide by structural doping with metallic bismuth, due to its ability to capture electrons formed in the photocatalytic process, which is comparable to the effect obtained by noble metals, such as gold and platinum [6,10,11].

Although the heterojunctions proposed above result in improved transport and separation of the photogenerated charges, photocatalysts can be further tailored to promote an even superior photocatalytic response, as they are still limited by: (i) reduced absorption of visible light, (ii) low surface area and (iii) inadequate porous structure [12–14]. One way to minimize these problems is to incorporate carbonaceous materials into the systems proposed above.

The use of carbon xerogel to increase the efficiency of photocatalyst has been previously reported in the literature [15–19]. This junction promotes a set of interesting modifications to the original

semiconductor, such as:

- Lower recombination rates between the electron-vacancy pair, due to the high electrical conductivity of the carbon xerogel, which can act as an electron sink;
- Increased adsorption of molecules, a fundamental step for photodegradation, due to a higher surface area and porosity;
- Increased visible light absorption;
- Modification in the crystallization process of the oxides.

Generally, carbon xerogels are obtained by evaporative drying of the product achieved from the catalyzed polycondensation of resorcinol with formaldehyde. As the cost of the starting materials constitutes 80% of the total production cost of the resorcinol-formaldehyde xerogel [20], an economically viable alternative can be found in the use of low cost carbon precursors, such as natural tannins extracted from tree barks. Black wattle tannin is a low-cost macromolecule with a polyhydroxyphenolic structure, which gives this compound suitable reactivity with formaldehyde [21].

Therefore, this work aims at the development of Bi-doped ZnO/ β -Bi₂O₃/Carbon xerogel composites for photocatalytic applications under solar and visible light. The photocatalytic response will be evaluated by the photodegradation of the 4-chlorophenol molecule, which is used here as a model molecule for the degradation of persistent organic pollutants (POP's).

2. Materials and methods

2.1. Preparation of the ZnO/Bi₂O₃/carbon xerogel composite

Firstly, 1 mL of nitric acid (HNO₃, 63% w/w) was added to a glass beaker, along with a pre-defined mass of bismuth nitrate (Bi(NO₃)₃, 98% w/w). After the Bi(NO₃)₃ dissolution, 50 mL of deionized water and 20 g of zinc nitrate (Zn(NO₃)₂, 98% w/w) were added to the system, under magnetic stirring. Then, 1 g of tannin (PHENOTAN BS) and 1 mL of formaldehyde (CH₂O, 37% w/w) were added to the beaker. Finally, 50 mL of a 0.32 mol L⁻¹ potassium hydroxide (KOH, 85% w/w) solution was added to the mixture, which was then kept under stirring for 15 min. The precipitate was washed with deionized water until the pH of the filtrate was neutral and dried in an oven at 100 °C until constant weight was obtained.

The resulting material was added to a closed crucible and calcined under nitrogen atmosphere at different temperatures (T_{calc} = 300 °C, 400 °C, 500 °C and 600 °C) for 1 h, with heating rate of 10 °C min⁻¹.

The theoretical ratio of ZnO/Bi₂O₃ was modified by the addition of greater amounts of Bi(NO₃)₃ during the synthesis pathway. The composites will be identified as XC/ZnO–Bi₂O₃ x%, where x% corresponds to the theoretical mass percentage of bismuth oxide (Bi₂O₃) in the composite. The list of reactants and quantities used for the preparation of each material is listed in Table 1.

Table 1
Reactants and quantities used for the preparation of each material.

Material	HNO3 (mL)	Zn(NO3)2 (g)	Bi(NO3)3 (g)	Tannin (g)	CH2O (ml)	KOH (g)
ZnO	1.0	20.0	–	–	–	9.0
ZnO–Bi ₂ O ₃ 5%	1.0	20.0	0.60	–	–	9.0
XC/ZnO	1.0	20.0	–	1.0	1.0	9.0
XC/ZnO–Bi ₂ O ₃ 1%	1.0	20.0	0.11	1.0	1.0	9.0
XC/ZnO–Bi ₂ O ₃ 2.5%	1.0	20.0	0.29	1.0	1.0	9.0
XC/ZnO–Bi ₂ O ₃ 5%	1.0	20.0	0.60	1.0	1.0	9.0
XC/ZnO–Bi ₂ O ₃ 7.5%	1.0	20.0	0.91	1.0	1.0	9.0
XC/ZnO–Bi ₂ O ₃ 10%	1.0	20.0	1.25	1.0	1.0	9.0
Bi ₂ O ₃	1.0	–	1.00	–	–	1.0

2.2. Characterization

The nitrogen isotherms were obtained at $-196\text{ }^{\circ}\text{C}$ in a V-Sorb 2800 adsorption analyzer (Gold APP Instruments). Before analysis, the materials were degassed under vacuum at $120\text{ }^{\circ}\text{C}$ for 2 h. The specific surface area was determined using the BET method.

The X-ray diffractometry was performed on a PANalytical X'Pert PRO MPD 3060 diffractometer using copper radiation. The FullProf Suite software was used to perform the Rietveld refinement. The XPS analysis was performed in a spherical VSW HA-100 analyzer using AlK α radiation ($h\nu = 1486.6\text{ eV}$) and a pass energy of 44 eV . The analyses were performed under low pressure ($2 \times 10^{-8}\text{ mbar}$).

Scanning electron micrographs were obtained using a scanning electron microscope equipped with a field emission gun (FEG-SEM), model TESCAN MIRA 3. Transmission electron micrographs were obtained using a JEOL JEM-2100 LaB $_6$ microscope operating at 200 kV , equipped with a Gatan 2K digital camera. The energy dispersive spectroscopy was performed on an Oxford INCA spectrometer coupled to a HITACHI TM-3000 scanning electron microscope.

The infrared spectroscopy was performed using a universal attenuated total reflectance sensor. The analyzes were conducted in a PerkinElmer Frontier spectrometer, operating in the region of 4000 to 600 cm^{-1} with a resolution of 4 cm^{-1} . For each analysis, 16 scans were performed. Diffuse reflectance analysis was carried out on a Shimadzu UV-2600 spectrophotometer, with an integrating sphere attachment. The range used in the tests was located in the region between 220 and 800 nm .

Chronoamperometry tests were performed on an Autolab Metrohm potentiostat (model PGSTAT204) using a 3-electrode electrochemical system in order to investigate the photocurrent generation. A porous microlayer of each sample was deposited on a rotating disk electrode (Pine Research, model AFE3T050PTPK), which was used along a platinum foil counter electrode and an Ag/AgCl reference electrode. The experiments were performed in a single compartment quartz electrochemical cell ($V = 0.2\text{ L}$), using a K_2SO_4 aqueous solution (0.1 mol L^{-1}) as the electrolyte. The photocurrent determination was performed using 0.8 V (vs Ag/AgCl), with an acquisition time of 0.1 s .

2.3. Photocatalytic evaluation

A jacketed reactor ($h = 10\text{ cm}$ and $d_i = 10\text{ cm}$) was used in the photocatalytic experiments. A 4-chlorophenol solution ($C_0 = 10\text{ mg L}^{-1}$, $V = 0.5\text{ L}$) was added to the reactor, along with 0.1 g of photocatalyst. The process was maintained at $25\text{ }^{\circ}\text{C}$ using water from a thermostatic bath. The photocatalyst was uniformly dispersed by magnetic stirring. The concentration of 4-chlorophenol in the system was determined spectrophotometrically on a Shimadzu UV-2600 spectrophotometer at the wavelength of 224 nm [16]. Prior to the photocatalytic experiments, the reactor was kept in the dark until the adsorption-desorption equilibrium was achieved. After that, the samples were exposed to an artificial radiation source (solar or visible). An Osram Ultra Vitalux 300 W lamp was used to simulate sunlight, whereas an OSRAM Powerstar 400 W lamp, with an UV filter, was used as a visible light source. Scavenging tests in the presence of isopropanol (scavenger for $\cdot\text{OH}$), nitrogen (O_2^- inhibitor, 0.3 L min^{-1}), sodium oxalate (scavenger for h^+ , 0.5 mol L^{-1}) and potassium chromate (scavenger for e^- , 0.025 mol L^{-1}) were performed in order to assess the photocatalytic mechanism involved in the process [16].

3. Results and discussion

3.1. Photocatalytic evaluation

Fig. 1 shows the results of the 4-chlorophenol photodegradation using the materials prepared under simulated solar radiation, varying the parameters of calcination temperature and ZnO/Bi $_2$ O $_3$ ratio.

First, it is noticeable that the XC/ZnO material has the highest photocatalytic activity at the calcination temperatures of 300 and $400\text{ }^{\circ}\text{C}$. In this temperature range, the addition of bismuth did not improve the photocatalytic properties of the XC/ZnO–Bi $_2$ O $_3$ x% materials, rendering them inferior to the XC/ZnO material. Furthermore, the XC/ZnO–Bi $_2$ O $_3$ 5% displayed the best photocatalytic response among its counterparts. Applying this same proportion to the oxide binary material (ZnO–Bi $_2$ O $_3$ 5%), it is evident that the efficiency of this material in comparison to the XC/ZnO–Bi $_2$ O $_3$ 5% is considerably lower, implying that carbon xerogel has a fundamental role in the photocatalytic efficiency of the XC/ZnO–Bi $_2$ O $_3$ x% composites.

However, the increase of calcination temperature to 500 and $600\text{ }^{\circ}\text{C}$ resulted in a significant improvement in the photocatalytic activity of the XC/ZnO–Bi $_2$ O $_3$ x% materials, when compared to the XC/ZnO, that displayed approximately the same efficiency in all temperatures tested. The XC/ZnO–Bi $_2$ O $_3$ 5% obtained the highest degradation of the 4-chlorophenol molecule at temperatures of 500 and $600\text{ }^{\circ}\text{C}$. Therefore, it is evident that the photoactivity of the XC/ZnO–Bi $_2$ O $_3$ x% materials depends strongly on the calcination temperature used, as well as on the ZnO/Bi $_2$ O $_3$ ratio used. The data obtained also show that the binary material ZnO–Bi $_2$ O $_3$ 5% continues to obtain a lesser degradation of 4-chlorophenol at higher calcination temperatures, confirming that the presence of carbon xerogel is extremely important to increase the photocatalytic activity of the composites. Furthermore, it is clear that the pure bismuth oxide is not an ideal photocatalyst for the degradation of 4-chlorophenol, as it achieved the worst degradation percentage among its counterparts. This is probably due to its high recombination rate and inadequate band structure [8,9,22].

A pseudo-first order kinetic model, based on the Langmuir-Hinshelwood equation, was used to fit the data obtained in the photocatalytic tests. This model is defined by Equation (1) [23]:

$$\ln\left(\frac{C_0}{C}\right) = k_{app}t \quad (1)$$

where C_0 is the concentration at the adsorption equilibrium and k_{app} is the apparent rate constant, which can be defined as the slope of the $\ln(C_0/C)$ versus t plot.

The kinetic data obtained using the proposed model is displayed in Table 2.

According to Table 2, the materials ZnO and XC/ZnO do not present significant variations in their values of apparent rate constant (k_{app}) with the variation of the calcination temperature, indicating that this factor has no significant influence on the photocatalytic efficiency of these materials. XC/ZnO–Bi $_2$ O $_3$ x% materials, on the other hand, have a strong link between calcination temperature and k_{app} , so that an increase in the calcination temperature causes a significant increase in the photocatalytic efficiency of the materials. The material XC/ZnO–Bi $_2$ O $_3$ 5%, calcined in $600\text{ }^{\circ}\text{C}$, obtained the highest k_{app} value among all tests performed.

Fig. 2 shows the results obtained in the visible radiation degradation tests, also varying the parameters of calcination temperature and ZnO/Bi $_2$ O $_3$ ratio.

It is noted that the behavior obtained for photocatalytic tests performed under visible radiation was similar to the one obtained in the solar tests, and the materials XC/ZnO–Bi $_2$ O $_3$ x% showed superior degradation capacity when calcined at higher temperatures. Once again, the material XC/ZnO–Bi $_2$ O $_3$ 5% calcined at $600\text{ }^{\circ}\text{C}$ achieved the highest degradation of 4-chlorophenol, confirming the calcination temperature of $600\text{ }^{\circ}\text{C}$ and the ZnO/Bi $_2$ O $_3$ ratio of this material as ideal for an optimized photocatalytic activity. Pure bismuth oxide showed no activity for the degradation of 4-chlorophenol under visible radiation.

The degradation kinetic of tests performed under visible radiation was also evaluated using the pseudo-first order model. The results are shown in Table 3.

The behavior of the k_{app} values for the visible radiation tests is similar to the one found in the solar radiation experiments, with the

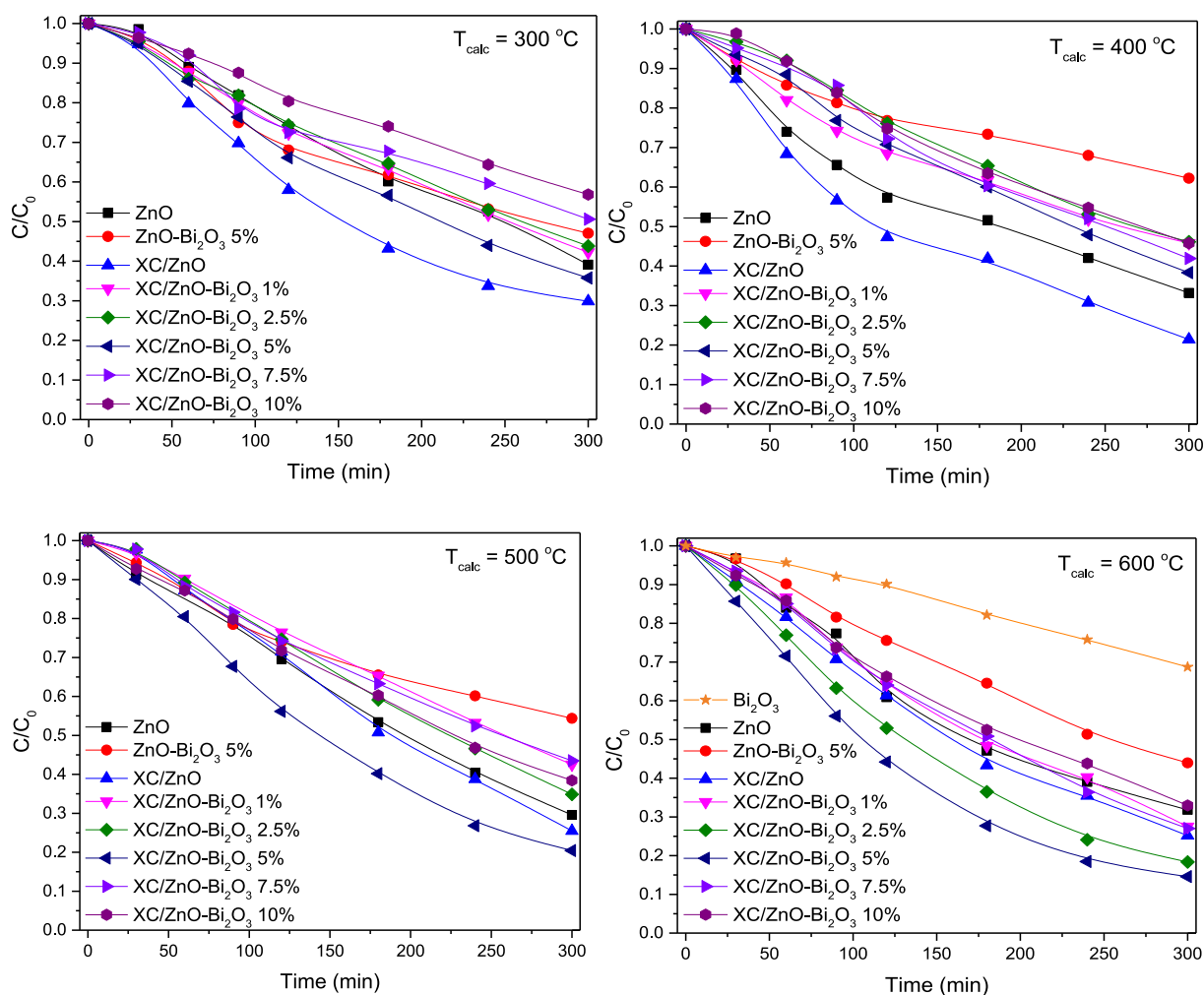


Fig. 1. Photodegradation results using the XC/ZnO–Bi₂O₃ x% materials calcined in different temperatures ($m_{cat} = 0.1$ g, $V = 0.5$ L, $C_0 = 10$ mg L⁻¹, Solar radiation).

maximum values found for the materials XC/ZnO–Bi₂O₃ x% calcined at 600 °C.

3.2. Characterization

As observed in the photocatalytic results, the degradation efficiency of the composites is strongly linked to the calcination temperature used. Therefore, Fig. 3 shows the effect of calcination temperature on the structural properties of the XC/ZnO–Bi₂O₃ 5% composite, evaluated by X-ray diffractometry.

According to Fig. 3, only the hexagonal zinc oxide phase is present

for the calcination temperatures of 300 and 400 °C. The peaks related to this phase are found at 2θ angles of: 31.9°, 34.6°, 36.4°, 47.5°, 56.6°, 63°, 66.3°, 68.1° and 69°, with the respective reflection planes: (1 0 0), (0 0 2), (1 0 1), (1 0 2), (1 1 0), (1 0 3), (2 0 0), (1 1 2) and (2 0 1) [23]. It is evident that the calcination process at lower temperatures was not able to crystallize any bismuth-based structure in the composite. Therefore, the bismuth fraction of the material is probably in an amorphous state.

Amorphous structures have a high level of disorder between their atoms, which leads to the creation of a large number of structural defects distributed in the material matrix. In the photocatalytic process,

Table 2
Kinetic data obtained using the pseudo-first order kinetic model ($k_{app} = [\text{min}^{-1}]$).

Material	T _{calc} = 300 °C		T _{calc} = 400 °C		T _{calc} = 500 °C		T _{calc} = 600 °C	
	k_{app}	R ²						
ZnO	0.0033	0.973	0.0038	0.974	0.0036	0.981	0.0037	0.983
ZnO–Bi ₂ O ₃ 5%	0.0020	0.978	0.0017	0.965	0.0022	0.979	0.0026	0.983
XC/ZnO	0.0043	0.985	0.0046	0.978	0.0044	0.969	0.0044	0.991
XC/ZnO–Bi ₂ O ₃ 1%	0.0027	0.991	0.0027	0.984	0.0029	0.976	0.0042	0.982
XC/ZnO–Bi ₂ O ₃ 2.5%	0.0026	0.990	0.0025	0.979	0.0032	0.964	0.0058	0.992
XC/ZnO–Bi ₂ O ₃ 5%	0.0030	0.992	0.0034	0.989	0.0052	0.989	0.0069	0.997
XC/ZnO–Bi ₂ O ₃ 7.5%	0.0022	0.980	0.0027	0.980	0.0031	0.985	0.0041	0.986
XC/ZnO–Bi ₂ O ₃ 10%	0.0018	0.988	0.0025	0.979	0.0030	0.987	0.0036	0.993
Bi ₂ O ₃	–	–	–	–	–	–	0.0012	0.987

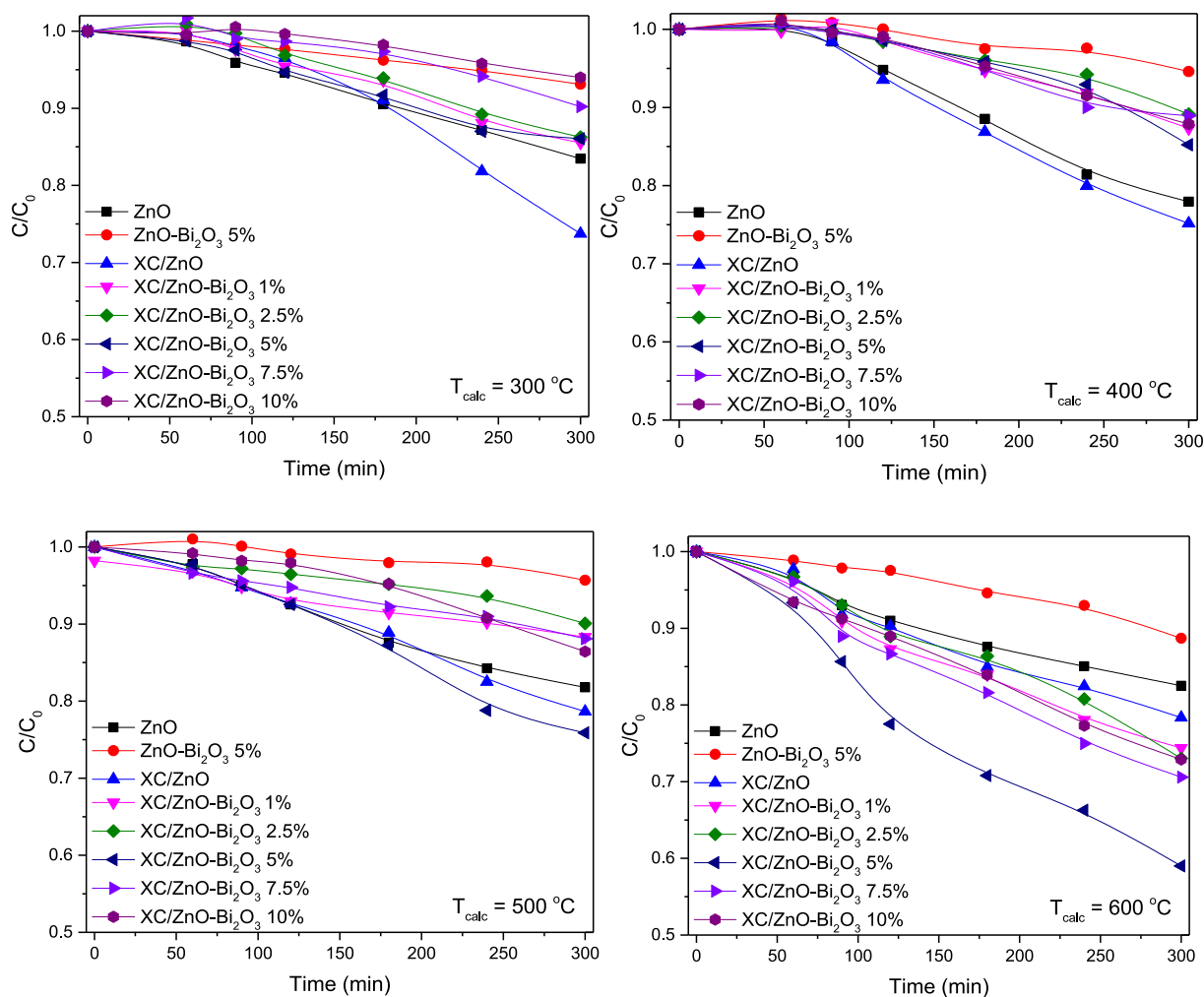


Fig. 2. Photodegradation results using the XC/ZnO–Bi₂O₃ x% materials calcined in different temperatures ($m_{cat} = 0.1$ g, $V = 0.5$ L, $C_0 = 10$ mg L⁻¹, Visible radiation).

these defects can function as centers for recombination of the photo-generated charges, which can significantly hinder the catalytic activity of a photocatalyst [24,25]. Xiao et al. [26] reported that the β -Bi₂O₃ phase exhibited superior photocatalytic activity when calcined at high temperatures, as the low crystallinity obtained at low temperatures caused a sharp drop in the oxide photoactivity. Thus, the decreased photocatalytic activity of the XC/ZnO–Bi₂O₃ w% in lower calcination temperatures can be linked to the high rate of charge recombination caused by structural defects in the amorphous bismuth phase.

However, at the calcination temperature of 500 °C, it is noticeable that a new phase is present. This phase corresponds to the tetragonal crystalline structure of bismuth oxide, also known as β -Bi₂O₃. The peaks

related to this phase can be found in the 2 θ positions of: 28°, 30.3°, 32.75°, 46.3° and 55.6°; with the respective reflection planes: (2 2 1), (3 1 1), (4 0 0), (4 0 2) and (6 2 1) [27]. The β -Bi₂O₃ phase is reported as a metastable phase of bismuth oxide, which transforms into the α -Bi₂O₃ phase when cooled. However, the presence carbon xerogel into the composite may be responsible for the stabilization of this phase at low temperatures, as this carbonaceous phase has been reported as responsible for the modification and structural stabilization of the TT phase of the niobium oxide at low temperatures [17].

The β -Bi₂O₃ phase is reported to possess the lower bandgap energy (2.4 eV) between the bismuth oxide allotropes, which is beneficial to the photocatalytic activity of the proposed composite [26].

Table 3

Kinetic data obtained using the pseudo-first order kinetic model ($k_{app} = [\text{min}^{-1}]$, Visible radiation).

Material	$T_{calc} = 300$ °C		$T_{calc} = 400$ °C		$T_{calc} = 500$ °C		$T_{calc} = 600$ °C	
	k_{app}	R ²						
ZnO	0.0008	0.997	0.0011	0.994	0.0009	0.986	0.0008	0.982
ZnO–Bi ₂ O ₃ 5%	0.0002	0.989	0.0003	0.944	0.0002	0.979	0.0004	0.963
XC/ZnO	0.0012	0.962	0.0012	0.998	0.0010	0.969	0.0009	0.977
XC/ZnO–Bi ₂ O ₃ 1%	0.0003	0.987	0.0006	0.962	0.0005	0.960	0.0010	0.987
XC/ZnO–Bi ₂ O ₃ 2.5%	0.0007	0.994	0.0005	0.955	0.0004	0.962	0.0011	0.975
XC/ZnO–Bi ₂ O ₃ 5%	0.0007	0.975	0.0007	0.959	0.0011	0.985	0.0018	0.981
XC/ZnO–Bi ₂ O ₃ 7.5%	0.0004	0.963	0.0006	0.969	0.0005	0.989	0.0012	0.988
XC/ZnO–Bi ₂ O ₃ 10%	0.0003	0.988	0.0006	0.987	0.0005	0.947	0.0011	0.995

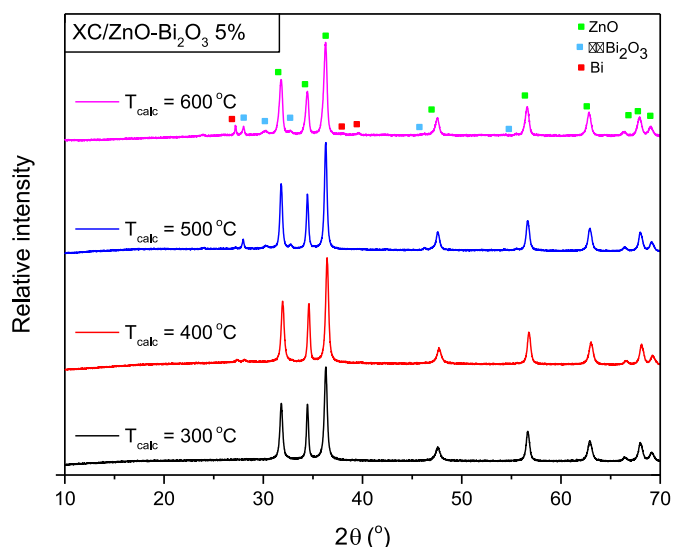
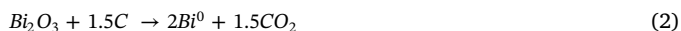


Fig. 3. Effect of calcination temperature on the structure of the XC/ZnO–Bi₂O₃ 5% composite.

Furthermore, as proposed in the Introduction section, the heterojunction between n-type (ZnO) and p-type (β -Bi₂O₃) semiconductors is related to a significant decrease in charge recombination, which results in enhanced photocatalytic activity [28]. Therefore, the effect of the p-n heterojunction between zinc oxide (ZnO) and bismuth oxide (β -Bi₂O₃) was probably responsible for the increase in photocatalytic activity of materials calcined at 500 °C.

Finally, for the calcination temperature of 600 °C, three distinct crystalline phases are present in the material structure. In addition to the hexagonal zinc oxide and tetragonal bismuth oxide phases, peaks related to the rhombohedral phase of metallic bismuth can be identified. These peaks are located at the 2θ positions of: 27.2°, 38.1° and 39.7°; with the respective reflection planes: (0 1 2), (1 0 4) and (1 1 0) [29].

The presence of the metallic bismuth phase can be explained by the reduction of the β -Bi₂O₃ phase in the presence of carbon at high temperatures. This type of behavior is reported in the literature and is expressed by Equations (2)–(4) [10,30].



Equations (2) and (3) represent the reduction of bismuth oxide in oxygen-rich and oxygen-poor atmospheres, respectively. Both are endothermic and spontaneous in the temperature range between 200 and 1300 °C. Equation (4) represents the oxidation of metallic bismuth in the presence of oxygen, which regenerates the reduced bismuth oxide. This reaction is exothermic and spontaneous in the temperature range between 25 and 1300 °C [30]. However, as the calcination process was carried out under nitrogen atmosphere, the oxidation of the metallic bismuth was probably inhibited to some extent.

The incorporation of the metallic bismuth phase into the photocatalyst is also advantageous for the optimization of photocatalytic efficiency, since the heterojunction between metal and semiconductor also facilitates the separation of the photogenerated charges [6,10,11].

Therefore, the increased photocatalytic activity of the XC/ZnO–Bi₂O₃ w% calcined at 600 °C can be ascribed to three types of heterojunctions, which occur simultaneously in the photocatalyst matrix:

- i) Semiconductor/carbonaceous material heterojunction between ZnO/ β -Bi₂O₃ and carbon xerogel
- ii) p-n semiconductor heterojunction between ZnO and β -Bi₂O₃
- iii) Metal-semiconductor heterojunction due to the presence of metallic bismuth.

Fig. 4-A shows the effect of the ZnO/Bi₂O₃ ratio on the crystalline structure of the XC/ZnO–Bi₂O₃ w% composites, calcined at 600 °C; Fig. 4-B shows a comparison between the diffractograms of the materials XC/ZnO–Bi₂O₃ 5%, XC/ZnO, ZnO–Bi₂O₃ 5% and ZnO, all calcined at 600 °C.

According to Fig. 4-A, the behavior found for materials with different ZnO/Bi₂O₃ ratios is similar to the one found for the previously evaluated XC/ZnO–Bi₂O₃ 5%. Thus, we can identify 3 phases present in the crystalline structure of the materials XC/ZnO–Bi₂O₃ x%: hexagonal phase of zinc oxide, tetragonal phase of bismuth oxide and rhombohedral phase of metallic bismuth.

In order to investigate the mass fractions of each crystalline component present in the photocatalyst, diffractograms were adjusted using the Rietveld refinement method. The results obtained for each material are shown in Table 4.

The values show that obtained the amount of metallic bismuth and bismuth oxide increases with the increase of the bismuth nitrate

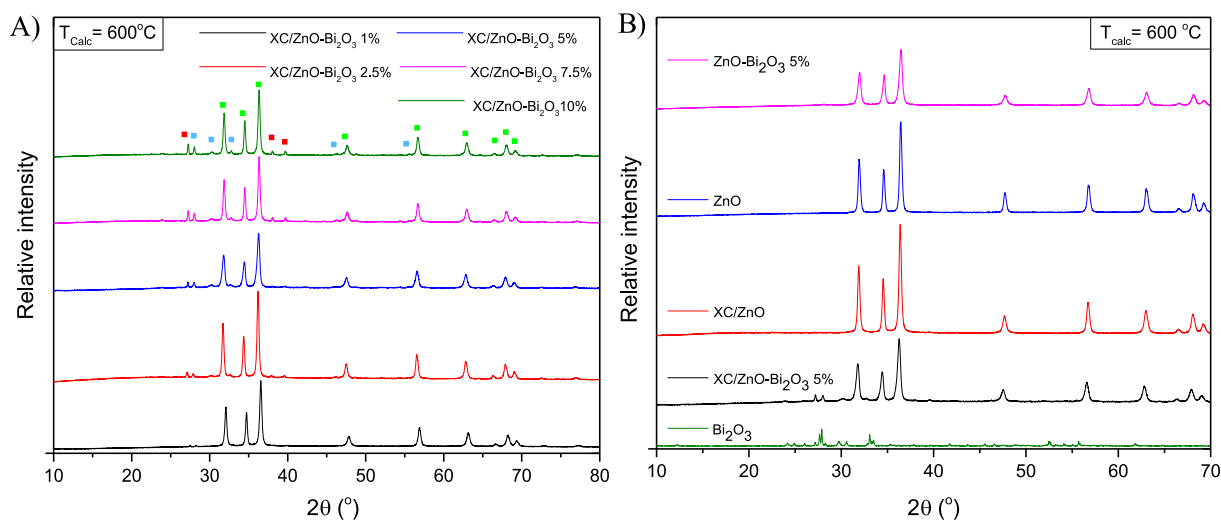


Fig. 4. A) Influence of ZnO/Bi₂O₃ ratio on the structure of the XC/ZnO–Bi₂O₃ x% B) Comparison of materials XC/ZnO–Bi₂O₃ 5%, XC/ZnO, ZnO–Bi₂O₃ 5% and ZnO (T_{calc} = 600 °C).

Table 4
Proportions obtained using the Rietveld refinement method.

Material	ZnO (% w/w)	β -Bi ₂ O ₃ (% w/w)	Bi ⁰ (% w/w)	χ^2
XC/ZnO–Bi ₂ O ₃ 2.5%	98.39	0.86	0.75	6.01
XC/ZnO–Bi ₂ O ₃ 5%	97.68	1.42	1.00	5.92
XC/ZnO–Bi ₂ O ₃ 7.5%	95.99	2.18	1.83	5.11
XC/ZnO–Bi ₂ O ₃ 10%	93.90	3.34	2.76	5.07

quantity used in the initial synthesis, as expected. It is also noticeable that the amount of bismuth oxide in the samples is always greater than the amount of metallic bismuth, displaying an overall ratio between these phases of approximately 0.55 β -Bi₂O₃/0.45 Bi⁰.

Literature reports that, in an isolated manner, bismuth oxide presents lower photoactivity than zinc oxide, due to a higher recombination rate of photogenerated charges [8,9,22]. Thus, the ideal ratio between ZnO and Bi₂O₃ should favor the effect of heterojunctions on the composite without negatively influencing its overall photocatalytic activity. Therefore, in this work, the proportion obtained in the XC/ZnO–Bi₂O₃ 5% composite is ideal to maximize the beneficial effect of the proposed modification.

As for Fig. 4-B, the materials XC/ZnO and ZnO displayed only the peaks related to the zinc oxide hexagonal structure, as expected. However, the material ZnO–Bi₂O₃ 5% did not show any peak relative to the bismuth phases present in the XC/ZnO–Bi₂O₃ 5% material, indicating that the entire mass fraction containing bismuth is still in an amorphous state. As previously discussed, the high number of defects in this type of structure leads to a high rate of charge recombination, which decreases the photocatalytic efficiency of the material. This factor, added to the lack of carbon/semiconductor heterojunctions in the material, explains the poor photocatalytic activity of the ZnO–Bi₂O₃ 5% in all photocatalytic tests. Furthermore, the importance of the carbon xerogel coupling is clear, as it was clearly responsible for the formation and stabilization of the β -Bi₂O₃ and Bi⁰ phases present in the XC/ZnO–Bi₂O₃ x% composites. The pure bismuth oxide presented the α -Bi₂O₃ structure, evidencing the effect of the carbon xerogel on the crystallization of the bismuth-based phases [31].

Fig. 5 shows the scanning electron micrographs obtained for the XC/ZnO–Bi₂O₃ 5%, XC/ZnO, ZnO–Bi₂O₃ 5% and ZnO, calcined at 600 °C.

Fig. 5-A shows that the zinc oxide (ZnO) is formed by spherical particle clusters, of approximately 100 nm. The XC/ZnO (Fig. 5-C) displays the same morphology, however, the size of the particles obtained is larger (\approx 150 nm), probably due to the incorporation of the carbon xerogel.

The material ZnO–Bi₂O₃ 5% (Fig. 5-B) is composed of spherical particles and rods, evidencing that the addition of bismuth severely affected the zinc oxide morphology. Finally, the material XC/ZnO–Bi₂O₃ 5% (Fig. 5-D) is composed mostly of particles equal to those found in the XC/ZnO. However, deformed particles (indicated by the red arrows) can be observed, indicating heterogeneity in the distribution of the phases present in the material.

Fig. 6 shows the transmission electron micrographs obtained for the XC/ZnO–Bi₂O₃ 5%.

Fig. 6A shows that the material XC/ZnO–Bi₂O₃ 5% is indeed composed of particles of spherical character (blue highlight) and distorted character (red highlight). The high resolution transmission electron micrograph of the spherical particles (Fig. 6-B) showed an interplanar distance of 0.26 nm, which is characteristic of the plane (0 0 2) of the hexagonal zinc oxide structure [16].

The elemental mapping of the XC/ZnO–Bi₂O₃ 5% ($T_{\text{calc}} = 600$ °C) obtained by energy dispersive spectroscopy is shown in Fig. 7.

Firstly, it is reasonable to say that the homogeneous carbon distribution indicates that the carbon xerogel is evenly distributed in the material matrix. This behavior provides the composite an optimized charge transfer between the heterojunctions of the semiconductor/

carbon phases, increasing the photocatalytic efficiency of the material [23]. Regarding the Bi⁰ and β -Bi₂O₃ phases, regions with high concentration of bismuth are scattered throughout the material, along with a homogeneously distributed amount of the element. The high concentration points are observed in the micrograph as regions of greater brightness, which is a characteristic behavior of metals deposited on a semiconductor's surface [32,33]. Thus, these regions correspond to concentrated points of the metallic bismuth distributed in the matrix of the XC/ZnO–Bi₂O₃ 5% composite, which corroborates the heterogeneity observed in the particle shapes of this material.

Fig. 8 shows the nitrogen isotherms for the materials XC/ZnO–Bi₂O₃ 5%, XC/ZnO, ZnO–Bi₂O₃ 5% and ZnO, all calcined at 600 °C.

According to the International Union of Pure and Applied Chemistry (IUPAC), the isotherms obtained for the all materials can be classified as type IV-H3. This type of isotherm has no adsorption limit at high P/P₀ values, indicating the presence of slit-shaped mesopores [34].

The Brunauer, Emmett and Teller (BET) relation was used to estimate the specific surface area of the materials. The total pore volume was calculated using the value found at the saturation point (P/P₀ = 0.99). The area and volume related to micropores were obtained using the t-plot technique. Table 5 shows the results obtained.

From the results obtained, one can notice a substantial increase in both specific surface area and pore volume of zinc oxide (ZnO) with the inclusion of bismuth in its structure (ZnO–Bi₂O₃ 5%). This result can be explained by the difference between the ionic radii of zinc and bismuth (0.74 and 1.17 Å, respectively), which can cause imperfections in the crystalline structure of the material and generate texturization of its surface, consequently increasing the specific surface area of the ZnO–Bi₂O₃ 5% [35]. The texturization of the ZnO–Bi₂O₃ 5% surface can be seen in the material's scanning electron micrograph (Fig. 5B), which showed a significant change in morphology when compared to pure ZnO.

The incorporation of the carbon xerogel caused an intense increase in the surface area and pore volume of the XC/ZnO composite. This behavior is expected, as the carbon xerogel has high surface area and porosity [36]. However, the addition of bismuth to this material caused a slight decrease in the values of specific surface area and micropore area. The micropore area of the material decreased in the same intensity as the total area, indicating that the micropores of the carbon network were filled by some component. Probably, the particles of metallic bismuth formed during calcination occupied these spaces, causing the observed behavior. Finally, the bismuth oxide displayed very low specific surface area and pore volume, which may also explain its poor photocatalytic efficiency.

Fig. 9 shows the pore size distribution for the materials XC/ZnO–Bi₂O₃ 5%, XC/ZnO, ZnO–Bi₂O₃ 5% and ZnO, calcined at 600 °C.

Regarding the macro and mesopore region (Fig. 9-A), we can see that the addition of the carbon xerogel to zinc oxide (XC/ZnO) resulted in an enhanced porous structure in the region of pore diameters between 25 and 160 nm, while the addition of bismuth (ZnO–Bi₂O₃ 5%) caused the a similar effect. Furthermore, Fig. 9-B shows that the materials without carbon in their composition displayed a negligible amount micropores, while the XC/ZnO material presented a more developed micropore structure, with average micropore diameter of 0.8 nm. As expected, the XC/ZnO–Bi₂O₃ 5% displayed an underdeveloped micropore structure, when compared to XC/ZnO, agreeing with the reduction in micropore volume and area previously observed.

Fig. 10-A shows the effect of the ZnO/Bi₂O₃ ratio on the diffuse reflectance spectra of the materials calcined at 600 °C, whereas Fig. 10-B shows the effect of the calcination temperature on the diffuse reflectance spectra of the XC/ZnO–Bi₂O₃ 5%.

Fig. 10-A shows that the ZnO–Bi₂O₃ 5% had a slight increase in its radiation absorption in the region between 400 and 500 nm, indicating that the addition of bismuth oxide resulted in a slight increase in visible light sensitivity of the material. The materials with carbon xerogel in their composition showed a considerably higher capacity for absorbing

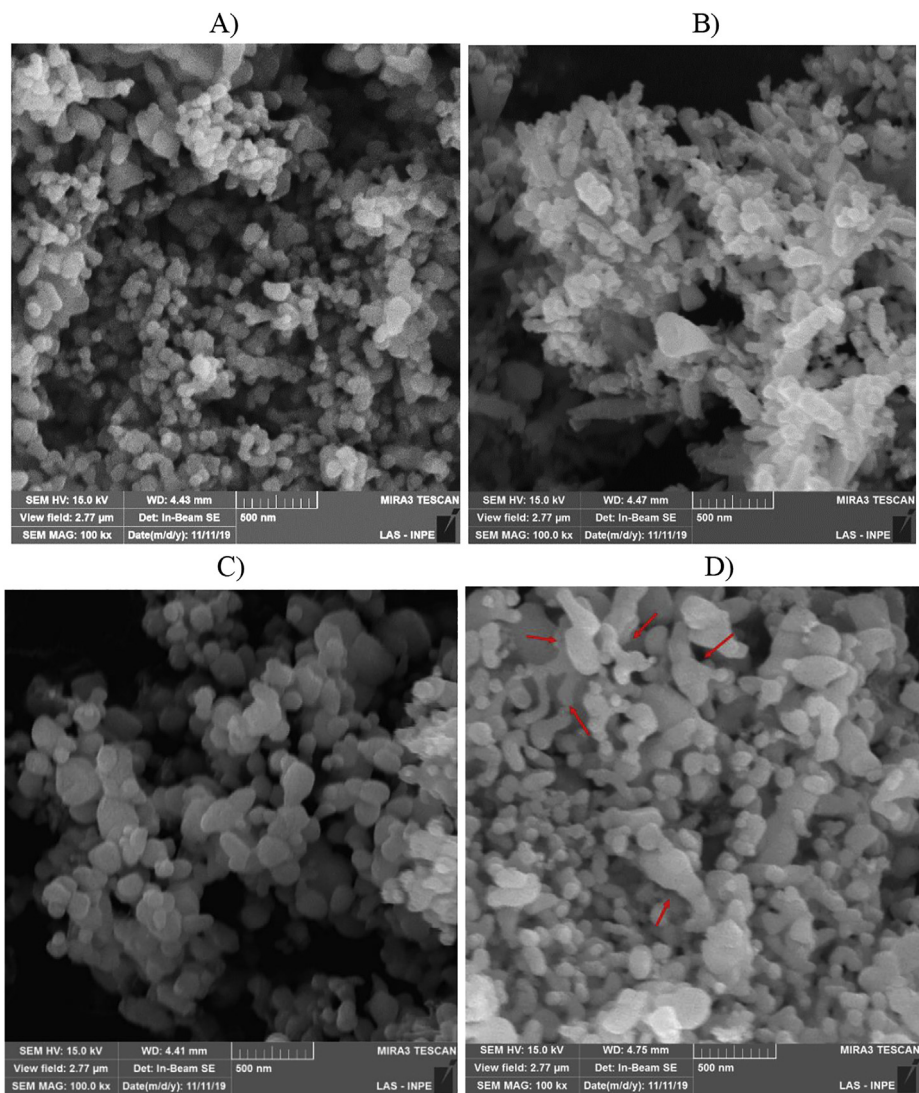


Fig. 5. Scanning electron micrographs (100000x, $T_{calc} = 600\text{ }^{\circ}\text{C}$) for the materials: A) ZnO; B) ZnO–Bi₂O₃; C) XC/ZnO; D) XC/ZnO–Bi₂O₃ 5%.

visible radiation, evidencing the synergy of the carbon/semiconductor heterojunction towards visible light harnessing. The variation in the ZnO/Bi₂O₃ ratio did not cause significant changes in the absorption spectrum of the materials, as the carbon xerogel absorption probably

masked the contribution of the bismuth phases. Furthermore, Fig. 10-B shows that an increase in the calcination temperature of the XC/ZnO–Bi₂O₃ 5% is linked to an increase in visible radiation absorption. As the visible light absorption is strongly linked to the carbon xerogel,

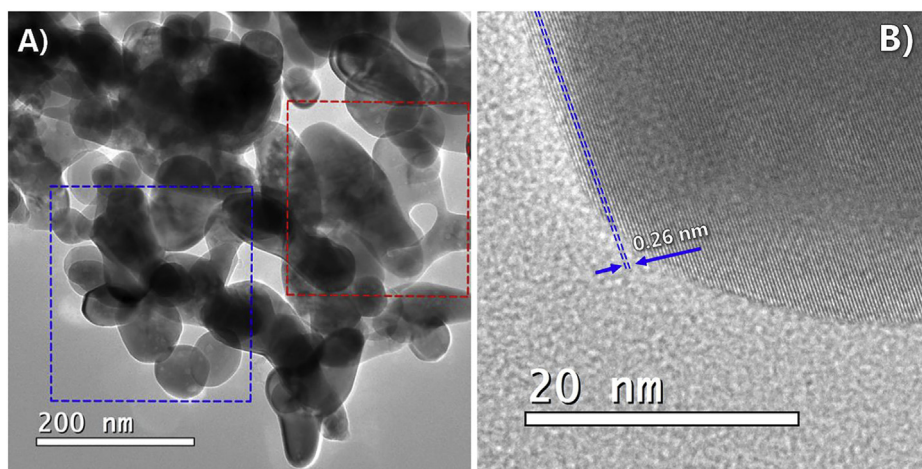


Fig. 6. Transmission electron micrographs for the XC/ZnO–Bi₂O₃ 5% ($T_{calc} = 600\text{ }^{\circ}\text{C}$): A) 200000x; B) 1500000x

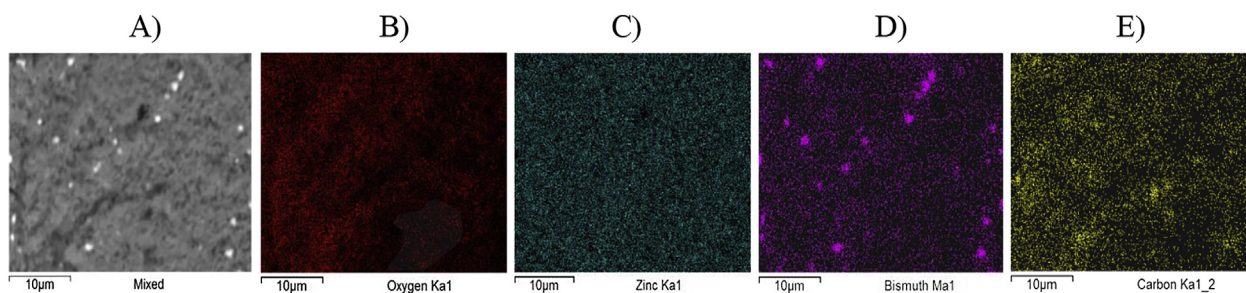


Fig. 7. Elemental mapping of the XC/ZnO–Bi₂O₃ 5% ($T_{\text{calc}} = 600\text{ }^{\circ}\text{C}$): A) Original micrograph; B) Oxygen; C) Zinc; D) Bismuth; E) Carbon.

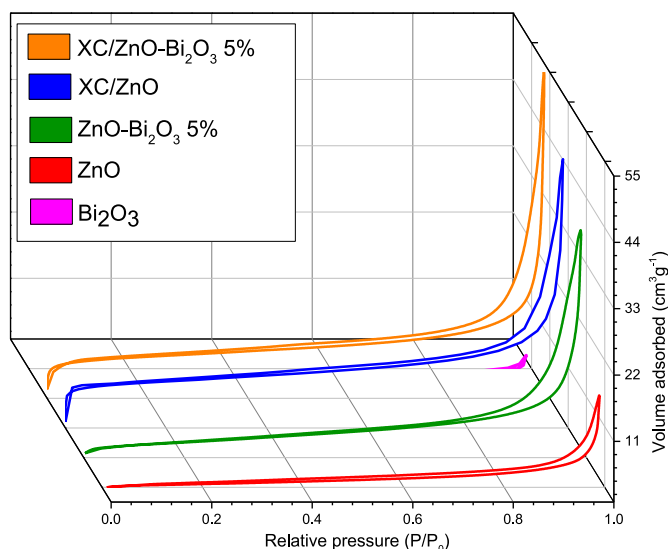


Fig. 8. Nitrogen isotherms for the materials XC/ZnO–Bi₂O₃ 5%, XC/ZnO, ZnO–Bi₂O₃ 5% and ZnO ($T_{\text{calc}} = 600\text{ }^{\circ}\text{C}$).

Table 5

Morphological parameters obtained for the XC/ZnO–Bi₂O₃ 5%, XC/ZnO, ZnO–Bi₂O₃ 5% and ZnO ($T_{\text{calc}} = 600\text{ }^{\circ}\text{C}$).

Material	Specific surface area ($\text{m}^2\text{ g}^{-1}$)	Micropore area ($\text{m}^2\text{ g}^{-1}$)	Pore volume ($\text{cm}^3\text{ g}^{-1}$)	Micropore volume ($\text{cm}^3\text{ g}^{-1}$)
XC/ZnO–Bi ₂ O ₃ 5%	27.11	15.91	0.086	0.0072
XC/ZnO	29.58	17.71	0.070	0.0082
ZnO–Bi ₂ O ₃ 5%	12.20	1.01	0.060	0.0005
ZnO	5.14	0.70	0.025	0.0003
Bi ₂ O ₃	0.51	0.20	0.005	0.0001

this result indicates that the calcination technique employed is particularly useful to prevent carbon loss from the composite matrix, as the carbon xerogel decomposition by heat treatment at high temperatures is reported as a disadvantageous characteristic of composites calcined under oxidizing atmosphere [23]. Literature also reports that an increase in the visible radiation absorption of a carbonaceous material is related to a facilitated charge transfer in its structure, which can also be linked to the greater photocatalytic efficiency achieved on higher calcination temperatures [37,38].

The methodology proposed by Ghobadi et al. was employed to calculate the gap energy of the materials prepared [39]. The results are displayed in Table 6.

The values obtained for all materials are characteristic of the zinc oxide gap energy, which is close to 3.2 eV [23]. The addition of the carbon xerogel resulted in a slight reduction in the bandgap energy of the materials, which may be caused by the incorporation of the carbonaceous structure into the zinc oxide crystalline structure [40]. The

calcination temperature had no significant effect on the bandgap energy of the XC/ZnO–Bi₂O₃ 5% composite, which was of approximately 3.18 eV in all temperatures tested. The gap energy of 2.8 eV found for the Bi₂O₃ agrees with the values reported in literature for the α -Bi₂O₃ structure [41].

Fig. 11 shows the X-ray photoelectron spectroscopy results for the XC/ZnO–Bi₂O₃ 5% composite, calcined at 600 °C.

Firstly, regarding the bismuth element, the deconvolution method was applied in order to identify four distinct peaks. The two peaks with the highest intensity, located at 164 and 158.7 eV, are related to the 4f_{5/2} and 4f_{7/2} orbitals of Bi³⁺, which is a characteristic behavior of bismuth oxide [42]. The peaks with lower intensity, located at 161.4 and 156.6 eV, are related to the 4f_{5/2} and 4f_{7/2} orbitals of Bi⁰ [10,42]. As for the zinc element, the peaks located at 1045 and 1021.3 eV are related to the 2p_{1/2} and 2p_{3/2} orbitals of the Zn²⁺, confirming the presence of zinc oxide in the composite [43].

The spectrum related to the carbon element can be deconvolved in 3 peaks. The peaks located at 285 and 289 eV are related to C–C and O–C=O bonds, respectively, which are present in the carbon xerogel structure. The peak at 286.4 eV is related to the Zn–O–C bond, confirming the chemical bonding between the carbon xerogel and the zinc oxide [23,44]. Finally, the spectrum related to oxygen can be deconvolved into 3 peaks. The peaks at 530.2 and 531.8 eV can be related to Zn–O and Bi–O bonds, respectively, whereas the peak at 532.5 eV can be related to the functional groups present in the carbon xerogel [23,45].

Fig. 12-A shows the effect of the ZnO/Bi₂O₃ ratio on the infrared spectrum of the materials calcined at 600 °C, whereas Fig. 12-B shows the effect of the calcination temperature on the infrared spectrum of the XC/ZnO–Bi₂O₃ 5%.

For all spectra obtained, the band between 3000 and 3500 cm⁻¹ is connected to the presence of carboxyl and phenolic groups, as well as adsorbed water. The vibrations of the Zn–O bonding are represented by the bands at 904 and 722 cm⁻¹ [23]. Regarding the carbonaceous phase, the bands around 1400–1450 and 1500 cm⁻¹ are related, respectively, to the C–H stretch of –CH₂ and –CH₃ groups and to the C=C bonds in aromatic structures. The band next to 1200 cm⁻¹ can be linked to the presence of ether-methylene bridges (C–O–C), formed during the polycondensation of the carbon xerogel [46,47]. Furthermore, at the calcination temperatures of 500 and 600 °C, a sharp band close to 840 cm⁻¹ can be noticed, which is characteristic of the Bi–O–C bond, indicating chemical interaction between the bismuth oxide and the carbon xerogel present in the composite [48].

3.3. Mechanism and stability evaluation

Fig. 13 shows the absorption spectra of the samples during the photocatalytic process using the photocatalyst XC/ZnO–Bi₂O₃ 5%, calcined at 600 °C.

It can be seen that there is a slight increase in absorption in the wavelength range between 240 and 260 nm, during the experiments. This behavior is explained by the creation of the intermediate 4-chlorocatechol, which absorbs radiation at the wavelength of 246 nm,

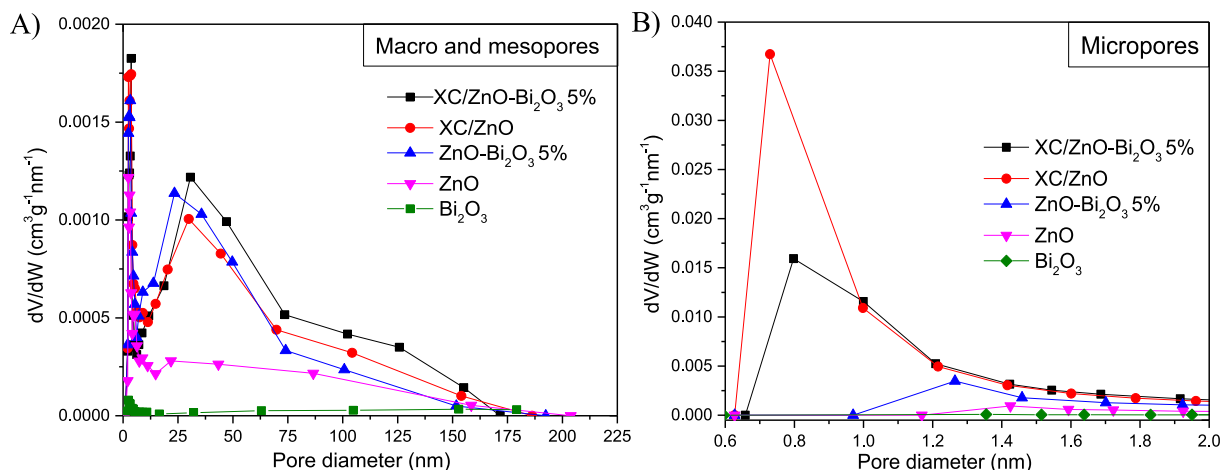


Fig. 9. Pore size distribution for the materials XC/ZnO-Bi₂O₃ 5%, XC/ZnO, ZnO-Bi₂O₃ 5% and ZnO (T_{calc} = 600 °C): A) Macro and mesopores; B) Micropores.

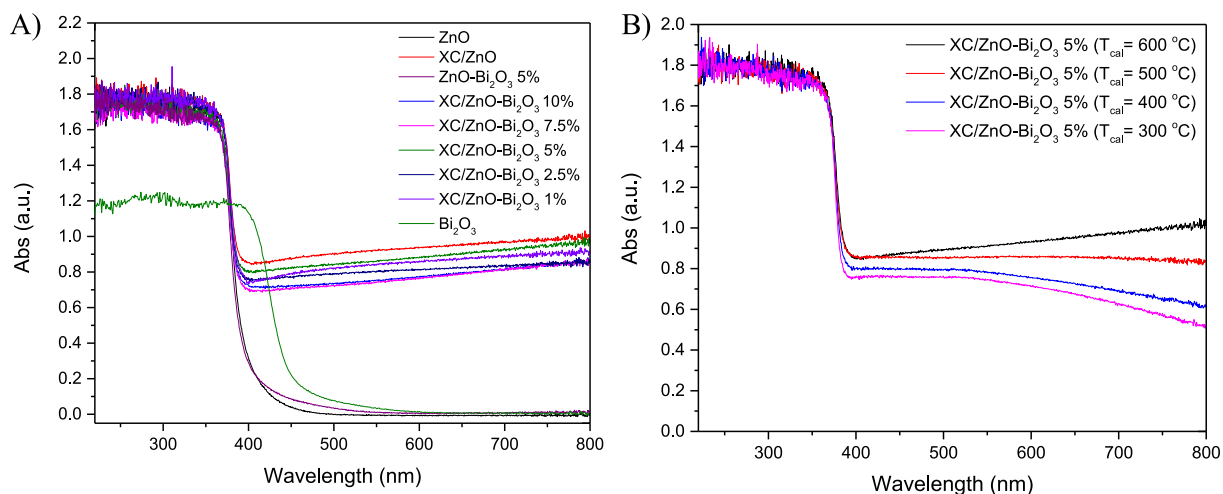


Fig. 10. Effect of: A) ZnO/Bi₂O₃ ratio on the diffuse reflectance spectra of the materials (T_{calc} = 600 °C); B) Calcination temperature on the diffuse reflectance spectra of the XC/ZnO-Bi₂O₃ 5%.

Table 6

Bandgap energies for the ZnO, XC/ZnO, ZnO-Bi₂O₃ 5% and XC/ZnO-Bi₂O₃ x% (T_{calc} = 600 °C).

Material	1/λ _{gap}	E _{gap} (eV)	Material	1/λ _{gap}	E _{gap} (eV)
ZnO	0.00259	3.21	XC/ZnO-Bi₂O₃ 2.5%	0.00257	3.18
Bi₂O₃	0.00226	2.80	XC/ZnO-Bi₂O₃ 5%	0.00257	3.18
XC/ZnO	0.00257	3.18	XC/ZnO-Bi₂O₃ 7.5%	0.00257	3.18
ZnO-Bi₂O₃ 5%	0.00258	3.20	XC/ZnO-Bi₂O₃ 10%	0.00257	3.18
XC/ZnO-Bi₂O₃ 1%	0.00257	3.18			

indicating that this is the main intermediate formed during the photocatalytic degradation of 4-chlorophenol [49]. Furthermore, the existence of this compound is no longer indicated in the spectra obtained at the end of the experiments, indicating that the intermediates were formed during the process and subsequently degraded.

According to literature, the main active radicals formed due to the photocatalytic effect are hydroxyl and superoxide radicals, in addition to the electron/vacancy pair formed by photonic excitation [16]. Thus, in order to study the influence of active radical formed during the photodegradation process, tests with scavengers were performed. The results obtained are shown in Fig. 14.

The results obtained show that the hydroxyl radical suppression has a major effect on the photocatalytic activity of all materials, which is in accordance with results found in the literature [23,50]. The superoxide radical also contributes to the degradation of pollutants, however with

less intensity. In view of the results obtained, the following mechanism for radical generation can be proposed (Equations (5)–(13)) [51,52].



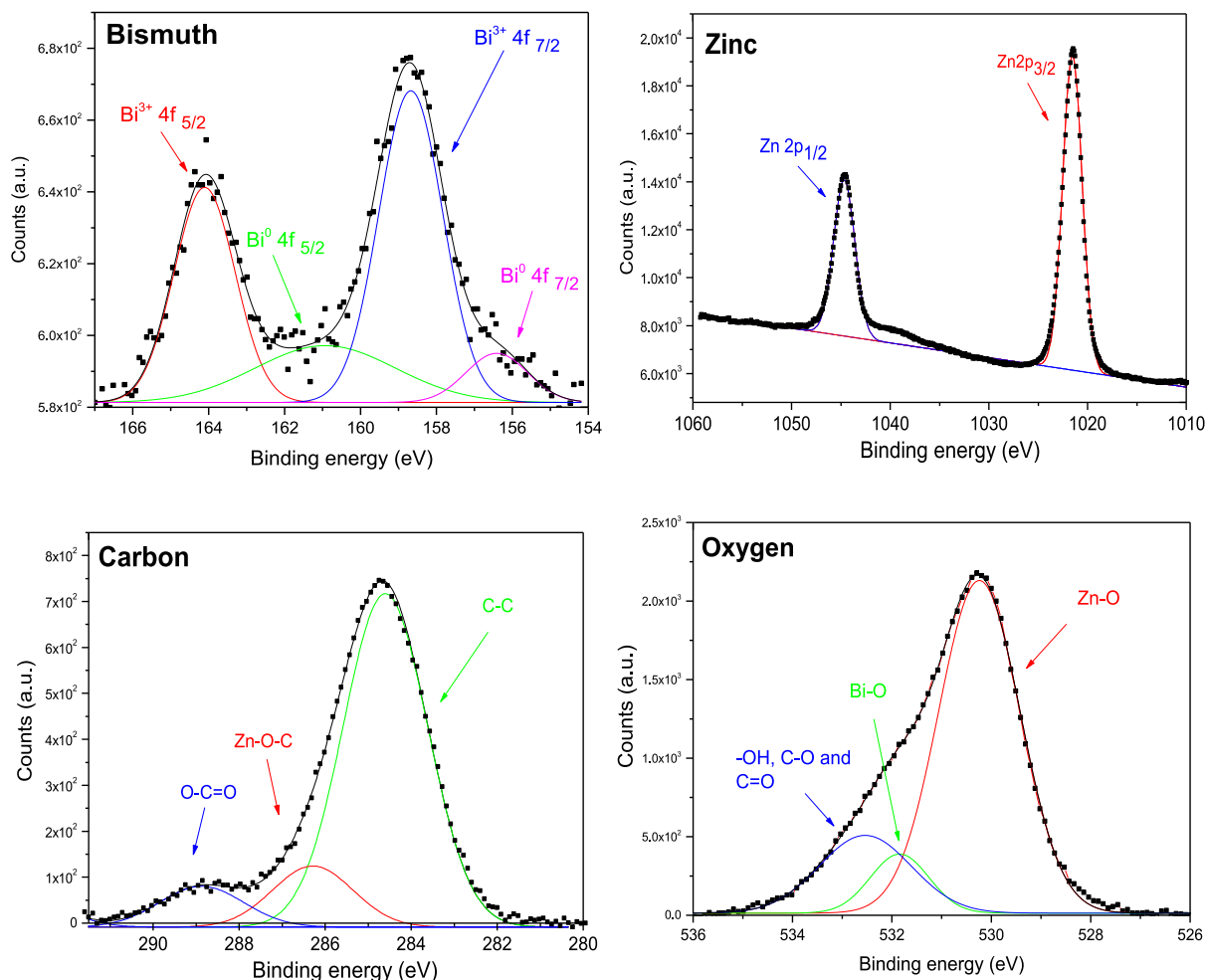


Fig. 11. X-ray photoelectron spectroscopy results for the XC/ZnO–Bi₂O₃ 5% composite ($T_{\text{calc}} = 600\text{ }^{\circ}\text{C}$).

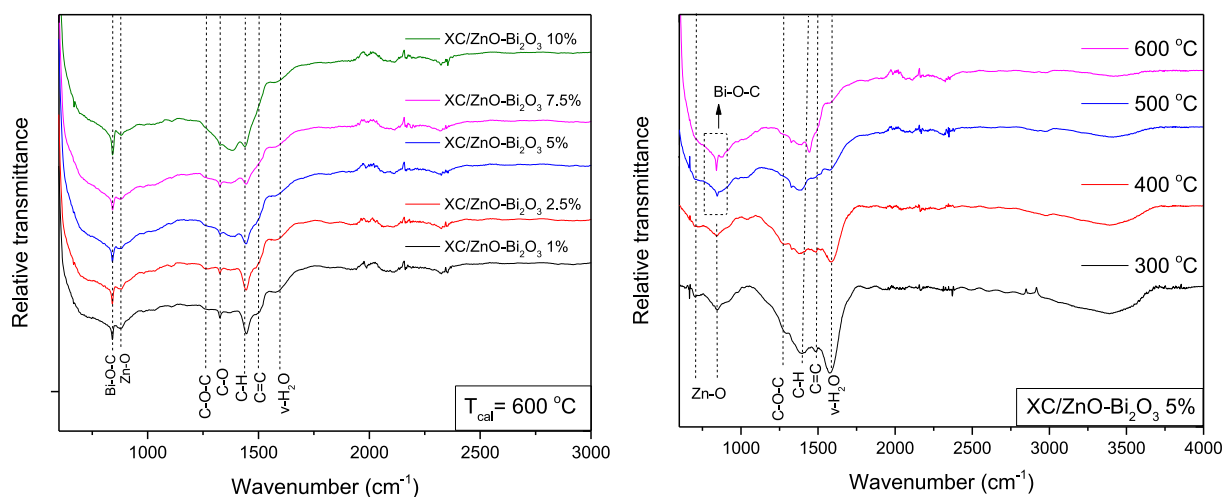


Fig. 12. A) Effect of the ZnO/Bi₂O₃ ratio on the infrared spectra of the materials ($T_{\text{calc}} = 600\text{ }^{\circ}\text{C}$); B) Effect of the calcination temperature on the infrared spectra of the XC/ZnO–Bi₂O₃ 5%.

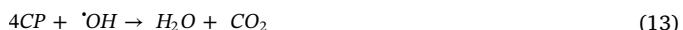


Fig. 15 shows the photocurrent generation under pulsed light irradiation for the materials prepared.

According to Fig. 16, the XC/ZnO–Bi₂O₃ 5% is able to generate a superior photocurrent density under visible light irradiation, which can be linked to its increased photocatalytic response. The recombination of

the photogenerated electron/vacancy pair dictates the photocurrent generation in a photocatalytic process, as higher charge recombination hinders the photocurrent generation [53,54]. Therefore, it can be said that the heterojunctions formed in the XC/ZnO–Bi₂O₃ 5% are responsible for diminishing the electron/vacancy pair recombination during the photocatalytic process, thus promoting increased charge

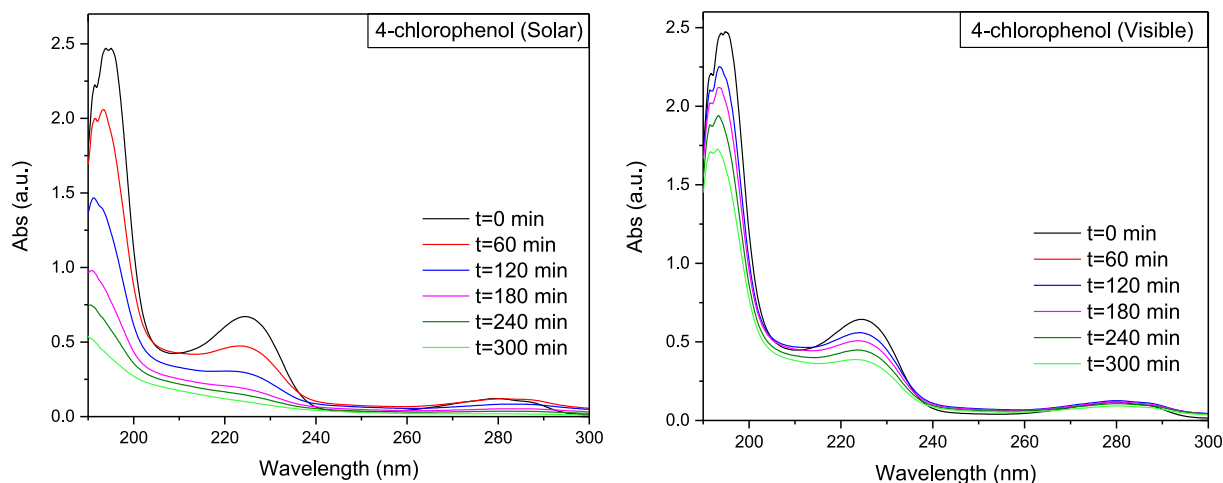


Fig. 13. Absorption spectrum of the 4-chlorophenol solution during the photocatalytic process using the photocatalyst XC/ZnO–Bi₂O₃ 5% (T_{calc} = 600 °C).

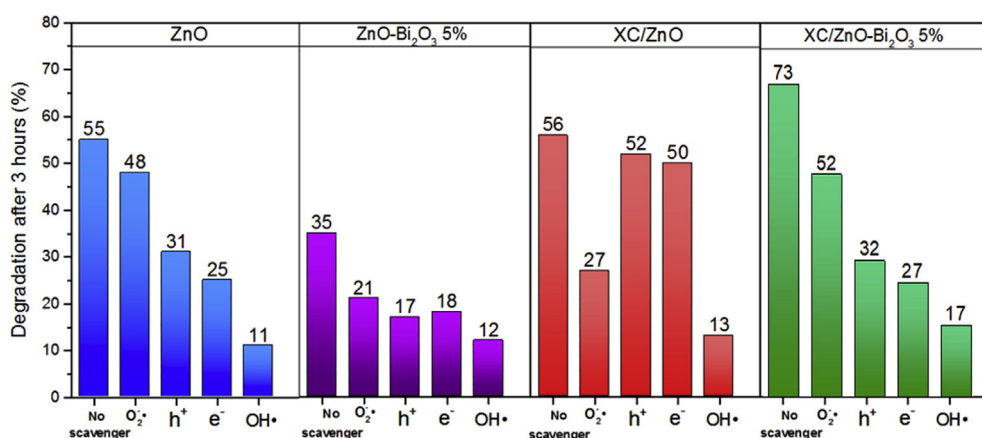


Fig. 14. Degradation obtained after 3 h using the scavenger methodology for the materials XC/ZnO–Bi₂O₃ 5%, XC/ZnO, ZnO–Bi₂O₃ 5% and ZnO (T_{calc} = 600 °C, Solar radiation).

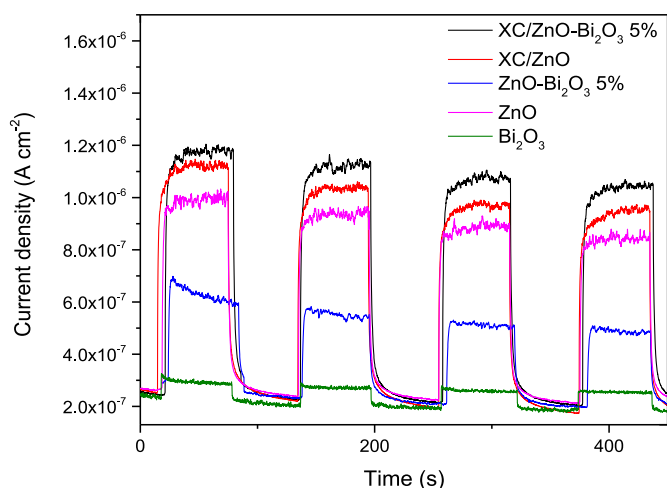


Fig. 15. Photocurrent generation under pulsed irradiation for the XC/ZnO–Bi₂O₃ 5%, XC/ZnO, ZnO–Bi₂O₃ 5% and ZnO (T_{calc} = 600 °C, Visible radiation).

transport and a consequential increase in photocatalytic efficiency.

The literature reports that the β-Bi₂O₃ has a conduction band potential (E_{CB}) of 0.22 eV and a valence band potential (E_{VB}) of 2.75 eV, whereas zinc oxide has E_{CB} = -0.3 eV and E_{VB} = 2.88 eV [55]. Due to the p-type nature of the β-Bi₂O₃, the value of Fermi level of this

semiconductor is close to its valence band potential. On the other hand, the Fermi level of the ZnO is higher than the one found in the β-Bi₂O₃ due to its n-type properties. After contact, the interface between these semiconductors will become electrically charged, due to the charge transfer caused by the Fermi level stabilization. Due to effect of the electric field, photogenerated electrons can be transferred from the CB of the semiconductor with lower fermi level (β-Bi₂O₃) to the CB of the semiconductor with higher Fermi level (ZnO), whereas vacancies will migrate in the opposite direction, moving from the ZnO VB to the β-Bi₂O₃ VB [55]. This separation will reduce the probability of charge recombination during the photocatalytic process and increase its overall efficiency. Considering the XC/ZnO–Bi₂O₃ w materials, the mechanism described above was further amplified by the presence of the carbon xerogel and metallic bismuth, which function as electron sinks for the photogenerated charges [6,11]. Therefore, Fig. 16 presents a schematic representation of the photocatalytic mechanism of the XC/ZnO–Bi₂O₃ w materials.

Finally, the stability of the XC/ZnO–Bi₂O₃ 5% was evaluated under recycle tests. For this purpose, the same sample of material was subjected to three photocatalytic cycles, being washed and dried at the end of each cycle. It is worth noting that the material used came from a second synthesis, different from the one used previously. The results are shown in Fig. 17.

The results show that the tested material maintained its photocatalytic efficiency during the three cycles, indicating a good stability for reuse applications. In addition, the results attest to the repeatability of the proposed methodology for the photocatalytic evaluation of the

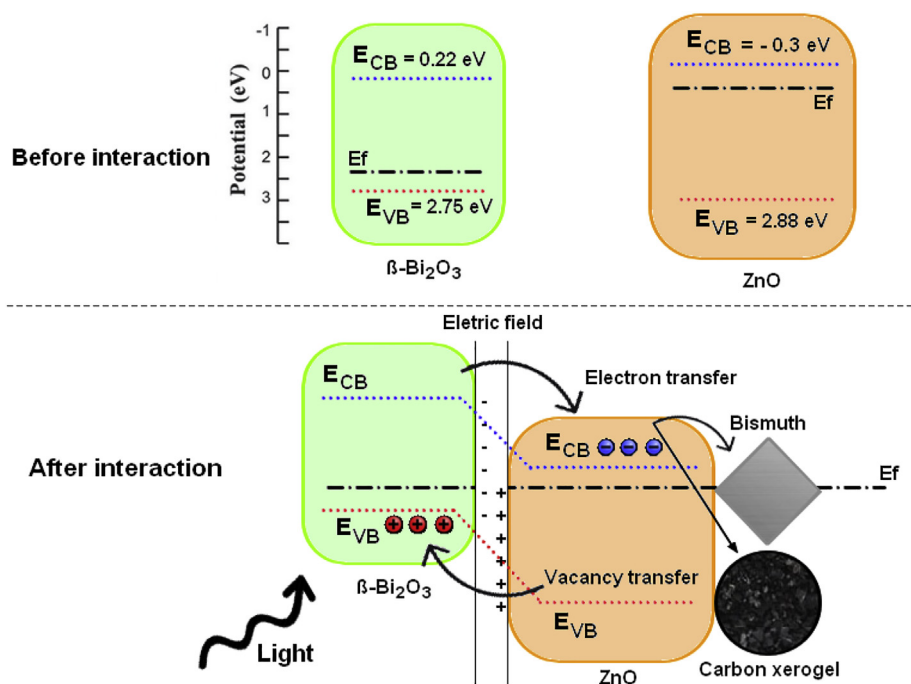


Fig. 16. Schematic representation of the photocatalytic process.

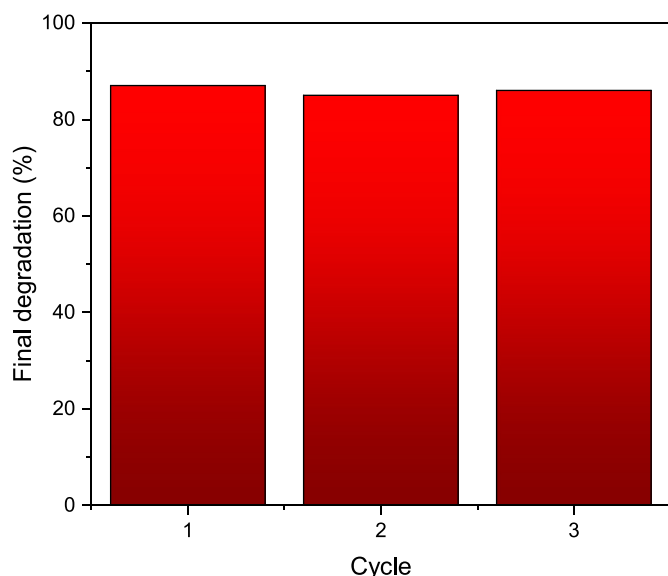


Fig. 17. Recycle test for the XC/ZnO–Bi₂O₃ 5%, ($T_{\text{calc}} = 600\text{ }^{\circ}\text{C}$, $m = 0.1\text{ g}$, $V = 0.5\text{ L}$, $C_0 = 10\text{ mg L}^{-1}$, Solar radiation).

materials and reproducibility of the proposed synthesis, since the results obtained here agree with the results shown previously.

4. Conclusion

In view of the results obtained in the work, it is evident that the calcination temperature is extremely important for the photocatalytic activity of the materials developed, due to its influence on the final structure of the composites. The highest photocatalytic efficiency was obtained at the calcination temperature of $600\text{ }^{\circ}\text{C}$, due to the formation of the $\beta\text{-Bi}_2\text{O}_3$ and Bi^0 phases, which enhanced photogenerated charge separation due to the formation of different types of heterojunction in the composite's structure. The XC/ZnO–Bi₂O₃ 5% composite displayed the highest photocatalytic activity among the material developed,

under visible and solar radiation. Regarding the photocatalytic mechanism, it was determined that the hydroxyl radical is the main active specie during the photocatalytic degradation of the 4-chlorophenol. Furthermore, the material has stability for reuse in photocatalytic processes and reproducibility of synthesis.

Declaration of competing interest

The authors declare that they have no known competing financial interests or personal relationships that could have appeared to influence the work reported in this paper.

Acknowledgments

The authors acknowledge the financial support provided by the São Paulo Research Foundation (Grants N^o 2018/10492-1, N^o 2018/12035-7, N^o 2017/10118-0, N^o 2013/02762-5 and N^o 2018/16360-0) and by the Conselho Nacional de Desenvolvimento Científico e Tecnológico (Grants N^o 155550/2018-7 and N^o 405543/2016-6). The authors are also grateful to TANAC S.A., which supplied the black wattle tannin.

References

- [1] S. Kang, L. Zhang, C. Yin, Y. Li, L. Cui, Y. Wang, Fast flash frozen synthesis of holey few-layer g-C₃N₄ with high enhancement of photocatalytic reactive oxygen species evolution under visible light irradiation, *Appl. Catal. B Environ.* 211 (2017) 266–274, <https://doi.org/10.1016/j.apcatb.2017.04.050>.
- [2] E. Basturk, M. Karatas, Decolorization of anthraquinone dye Reactive Blue 181 solution by UV/H₂O₂ process, *J. Photochem. Photobiol. A Chem.* 299 (2015) 67–72, <https://doi.org/10.1016/j.jphotochem.2014.11.003>.
- [3] S.M. Lam, J.C. Sin, I. Satoshi, A.Z. Abdullah, A.R. Mohamed, Enhanced sunlight photocatalytic performance over Nb₂O₅/ZnO nanorod composites and the mechanism study, *Appl. Catal. A Gen.* 471 (2014) 126–135, <https://doi.org/10.1016/j.apcata.2013.12.001>.
- [4] S.A. Mahmoud, O.A. Fouad, Synthesis and application of zinc/tin oxide nanostructures in photocatalysis and dye sensitized solar cells, *Sol. Energy Mater. Sol. Cells* 136 (2015) 38–43, <https://doi.org/10.1016/j.solmat.2014.12.035>.
- [5] K.M. Lee, C.W. Lai, K.S. Ngai, J.C. Juan, Recent developments of zinc oxide based photocatalyst in water treatment technology: a review, *Water Res.* 88 (2016) 428–448, <https://doi.org/10.1016/j.watres.2015.09.045>.
- [6] H. Wang, L. Zhang, Z. Chen, J. Hu, S. Li, Z. Wang, J. Liu, X. Wang, Semiconductor heterojunction photocatalysts: design, construction, and photocatalytic performances, *Chem. Soc. Rev.* 43 (2014) 5234–5244, <https://doi.org/10.1039/>

- c4cs00126e.
- [7] J. Wang, Y. Xia, H. Zhao, G. Wang, L. Xiang, J. Xu, S. Komarneni, Oxygen defects-mediated Z-scheme charge separation in $g\text{-C}_3\text{N}_4/\text{ZnO}$ photocatalysts for enhanced visible-light degradation of 4-chlorophenol and hydrogen evolution, *Appl. Catal. B Environ.* 206 (2017) 406–416, <https://doi.org/10.1016/j.apcatb.2017.01.067>.
- [8] X. Wang, P. Ren, H. Fan, Room-temperature solid state synthesis of $\text{ZnO}/\text{Bi}_2\text{O}_3$ heterojunction and their solar light photocatalytic performance, *Mater. Res. Bull.* 64 (2015) 82–87, <https://doi.org/10.1016/j.matresbull.2014.12.037>.
- [9] J.C. Medina, N.S. Portillo-Vélez, M. Bizarro, A. Hernández-Gordillo, S.E. Rodil, Synergistic effect of supported $\text{ZnO}/\text{Bi}_2\text{O}_3$ heterojunctions for photocatalysis under visible light, *Dyes Pigments* 153 (2018) 106–116, <https://doi.org/10.1016/j.dyepig.2018.02.006>.
- [10] L. Zhang, P. Ghimire, J. Phuriragpitikhon, B. Jiang, A.A.S. Gonçalves, M. Jaroniec, Facile formation of metallic bismuth/bismuth oxide heterojunction on porous carbon with enhanced photocatalytic activity, *J. Colloid Interface Sci.* 513 (2018) 82–91, <https://doi.org/10.1016/j.jcis.2017.11.011>.
- [11] F. Tian, H. Zhao, G. Li, Z. Dai, Y. Liu, R. Chen, Modification with metallic bismuth as efficient strategy for the promotion of photocatalysis: the case of bismuth phosphate, *ChemSusChem* 9 (2016) 1579–1585, <https://doi.org/10.1002/cssc.201600489>.
- [12] F. Chen, Q. Yang, S. Wang, F. Yao, J. Sun, Y. Wang, C. Zhang, X. Li, C. Niu, D. Wang, G. Zeng, Graphene oxide and carbon nitride nanosheets co-modified silver chromate nanoparticles with enhanced visible-light photoactivity and anti-photocorrosion properties towards multiple refractory pollutants degradation, *Appl. Catal. B Environ.* 209 (2017) 493–505, <https://doi.org/10.1016/j.apcatb.2017.03.026>.
- [13] X. Miao, X. Yue, Z. Ji, X. Shen, H. Zhou, M. Liu, K. Xu, J. Zhu, X. Yue, Z. Ji, L. Kong, X. Miao, H. Zhou, G. Zhu, S.A. Shah, X. Shen, Nitrogen-doped carbon dots decorated on $g\text{-C}_3\text{N}_4/\text{Ag}_3\text{PO}_4$ photocatalyst with improved visible light photocatalytic activity and mechanism insight, *Appl. Catal. B Environ.* 227 (2018) 459–469, <https://doi.org/10.1016/j.apcatb.2018.01.057>.
- [14] H. Wang, X. Liu, S. Wang, L. Li, Dual templating fabrication of hierarchical porous three-dimensional ZnO/carbon nanocomposites for enhanced photocatalytic and photoelectrochemical activity, *Appl. Catal. B Environ.* 222 (2018) 209–218, <https://doi.org/10.1016/j.apcatb.2017.10.012>.
- [15] N.P. de Moraes, C.A.S.H. de Azeredo, L.A.L.A. Bacetto, M.L.C.P. da Silva, L.A. Rodrigues, N.P. Moraes, C.A.S.H. de Azeredo, L.A.L.A. Bacetto, M.L.C.P. da Silva, L.A. Rodrigues, The effect of C-doping on the properties and photocatalytic activity of ZrO_2 prepared via sol-gel route, *Optik (Stuttg.)* 165 (2018) 302–309, <https://doi.org/10.1016/j.ijleo.2018.03.133>.
- [16] N.P. de Moraes, R.B. Valim, R. da Silva Rocha, M.L.C.P. da Silva, T.M.B. Campos, G.P. Thim, L.A. Rodrigues, Effect of synthesis medium on structural and photocatalytic properties of ZnO/carbon xerogel composites for solar and visible light degradation of 4-chlorophenol and bisphenol A, *Colloid. Surface. Physicochem. Eng. Aspect.* 584 (2020) 124034, <https://doi.org/10.1016/j.colsurfa.2019.124034>.
- [17] N.P. Moraes, R. Bacani, M. Lucia, C. Pinto, N.P. de Moraes, R. Bacani, M.L.C.P. da Silva, T.M.B. Campos, G.P. Thim, L.A. Rodrigues, Effect of Nb/C ratio in the morphological, structural, optical and photocatalytic properties of novel and inexpensive $\text{Nb}_2\text{O}_5/\text{carbon}$ xerogel composites, *Ceram. Int.* 44 (2018) 6645–6652, <https://doi.org/10.1016/j.ceramint.2018.01.073>.
- [18] E. Bailón-García, A. Elmouwahidi, M.A. Álvarez, F. Carrasco-Marín, A.F. Pérez-Cadenas, F.J. Maldonado-Hódar, New carbon xerogel- TiO_2 composites with high performance as visible-light photocatalysts for dye mineralization, *Appl. Catal. B Environ.* 201 (2017) 29–40, <https://doi.org/10.1016/j.apcatb.2016.08.015>.
- [19] N.P. de Moraes, M.L.C.P. da Silva, T.M.B. Campos, G.P. Thim, L.A. Rodrigues, N. Perciani, D.M. Maria, L. Caetano, S. Tiago, M. Bastos, G. Patrocínio, T. Liana, A. Rodrigues, Novel synthetic route for low-cost carbon-modified TiO_2 with enhanced visible light photocatalytic activity: carbon content and calcination effects, *J. Sol. Gel Sci. Technol.* 87 (2018) 380–390, <https://doi.org/10.1007/s10971-018-4700-4>.
- [20] K. Kraiwattanawong, S.R. Mukai, H. Tamon, A.W. Lothongkum, Control of mesoporous properties of carbon cryogels prepared from wattle tannin and furfural, *J. Porous Mater.* 15 (2008) 695–703, <https://doi.org/10.1007/s10934-007-9155-x>.
- [21] A. Szczyrek, G. Amaral-Labat, V. Fierro, A. Pizzi, A. Celzard, The use of tannin to prepare carbon gels. Part II. Carbon cryogels, *Carbon N. Y.* 49 (2011) 2785–2794, <https://doi.org/10.1016/j.carbon.2011.03.005>.
- [22] I. Benyamina, K. Manseri, M. Mansour, B. Benalioua, A. Bentouami, B. Boury, New $\text{Bi}_2\text{O}_3\text{-ZnO}$ composite deposited on glass wool. Effect of the synthesis method on photocatalytic efficiency under visible light, *Appl. Surf. Sci.* 483 (2019) 859–869, <https://doi.org/10.1016/j.apsusc.2019.03.310>.
- [23] N.P. de Moraes, L.A. Bacetto, G.S. dos Santos, M.L.C. Pinto da Silva, J.P.B. Machado, T.M.B. Campos, G.P. Thim, L.A. Rodrigues, Synthesis of novel ZnO/carbon xerogel composites: effect of carbon content and calcination temperature on their structural and photocatalytic properties, *Ceram. Int.* 45 (2019) 3657–3667, <https://doi.org/10.1016/j.ceramint.2018.11.027>.
- [24] X. Li, Y. Sun, T. Xiong, G. Jiang, Y. Zhang, Z. Wu, F. Dong, Activation of amorphous bismuth oxide via plasmonic Bi metal for efficient visible-light photocatalysis, *J. Catal.* 352 (2017) 102–112, <https://doi.org/10.1016/j.jcat.2017.04.025>.
- [25] Y. Zhang, L. Shi, Z. Geng, T. Ren, Z. Yang, The improvement of photocatalysis O_2 production over BiVO_4 with amorphous FeOOH shell modification, *Sci. Rep.* 9 (2019) 19090, <https://doi.org/10.1038/s41598-019-54940-2>.
- [26] X. Xiao, R. Hu, C. Liu, C. Xing, C. Qian, X. Zuo, J. Nan, L. Wang, Facile large-scale synthesis of $\beta\text{-Bi}_2\text{O}_3$ nanospheres as a highly efficient photocatalyst for the degradation of acetaminophen under visible light irradiation, *Appl. Catal. B Environ.* 140–141 (2013) 433–443, <https://doi.org/10.1016/j.apcatb.2013.04.037>.
- [27] X. Liu, W. Bian, C. Tian, Morphology, structure and optical properties of 3D Bi_2O_3 hierarchical architectures, *Mater. Lett.* 112 (2013) 1–4, <https://doi.org/10.1016/j.matlet.2013.08.107>.
- [28] G. Cai, L. Xu, B. Wei, J. Che, H. Gao, W. Sun, Facile synthesis of $\beta\text{-Bi}_2\text{O}_3/\text{Bi}_2\text{O}_3$ 2CO_3 nanocomposite with high visible-light photocatalytic activity, *Mater. Lett.* 120 (2014) 1–4, <https://doi.org/10.1016/j.matlet.2014.01.027>.
- [29] R.A. Patil, M.K. Wei, P.H. Yeh, J.B. Liang, W.T. Gao, J.H. Lin, Y. Liou, Y.R. Ma, Size-controllable synthesis of $\text{Bi}/\text{Bi}_2\text{O}_3$ heterojunction nanoparticles using pulsed Nd:YAG laser deposition and metal-semiconductor-heterojunction-assisted photoluminescence, *Nanoscale* 8 (2016) 3565–3571, <https://doi.org/10.1039/c5nr08417b>.
- [30] M.M. Sarafraz, M. Jafarian, M. Arjomandi, G.J. Nathan, Experimental investigation of the reduction of liquid bismuth oxide with graphite, *Fuel Process. Technol.* 188 (2019) 110–117, <https://doi.org/10.1016/j.fuproc.2019.02.015>.
- [31] H. Oudghiri-Hassani, S. Rakass, F.T. Al Wadaani, K.J. Al-Ghamdi, A. Omer, M. Messali, M. Abboudi, Synthesis, characterization and photocatalytic activity of $\alpha\text{-Bi}_2\text{O}_3$ nanoparticles, *J. Taibah Univ. Sci.* 9 (2015) 508–512, <https://doi.org/10.1016/j.jtusc.2015.01.009>.
- [32] T.K. Pathak, R.E. Kroon, V. Graciani, M. Popa, M.C. Chifiriuc, H.C. Swart, Influence of Ag, Au and Pd noble metals doping on structural, optical and antimicrobial properties of zinc oxide and titanium dioxide nanomaterials, *Heliyon* 5 (2019), <https://doi.org/10.1016/j.heliyon.2019.e01333>.
- [33] M.A. Ahmed, Z.M. Abou-Gamra, M.A. Alshakhanbeh, H. Medien, Control synthesis of metallic gold nanoparticles homogeneously distributed on hexagonal ZnO nanoparticles for photocatalytic degradation of methylene blue dye, *Environ. Nanotechnol. Mon. Manag.* 12 (2019) 100217, <https://doi.org/10.1016/j.enmm.2019.100217>.
- [34] Z.A. Allothman, A review: fundamental aspects of silicate mesoporous materials, *Materials (Basel)* 5 (2012) 2874–2902, <https://doi.org/10.3390/ma5122874>.
- [35] J.A. Oliveira, M.O. Reis, M.S. Pires, L.A.M. Ruotolo, T.C. Ramalho, C.R. Oliveira, L.C.T. Lacerda, F.G.E. Nogueira, Zn-doped Nb_2O_5 photocatalysts driven by visible-light: an experimental and theoretical study, *Mater. Chem. Phys.* 228 (2019) 160–167, <https://doi.org/10.1016/j.matchemphys.2019.02.062>.
- [36] G. Amaral-Labat, L.L. Grishchko, V. Fierro, B.N. Kuznetsov, A. Pizzi, A. Celzard, Tannin-based xerogels with distinctive porous structures, *Biomass Bioenergy* 56 (2013) 437–445, <https://doi.org/10.1016/j.biombioe.2013.06.001>.
- [37] K. Micheal, A. Ayeshamariam, S. Devanesan, K. Bhuvaneshwari, T. Pazhanivel, M.S. AlSalhi, M.J. Aljaafreh, Environmental friendly synthesis of carbon nanoplates supported ZnO nanorods for enhanced degradation of dyes and organic pollutants with visible light driven photocatalytic performance, *J. King Saud Univ. Sci.* 32 (2019) 1081–1087, <https://doi.org/10.1016/j.jksus.2019.10.003>.
- [38] B.R. Bunes, M. Xu, Y. Zhang, D.E. Gross, A. Saha, D.L. Jacobs, X. Yang, J.S. Moore, L. Zang, Photodoping and enhanced visible light absorption in single-walled carbon nanotubes functionalized with a wide band gap oligomer, *Adv. Mater.* 27 (2015) 162–167, <https://doi.org/10.1002/adma.201404112>.
- [39] N. Ghobadi, Band gap determination using absorption spectrum fitting procedure, *Int. Nano Lett.* 3 (2013) 2, <https://doi.org/10.1186/2228-5326-3-2>.
- [40] A.B. Lavand, Y.S. Malghe, Synthesis, characterization and visible light photocatalytic activity of carbon and iron modified ZnO , *J. King Saud Univ. Sci.* 30 (2018) 65–74, <https://doi.org/10.1016/j.jksus.2016.08.009>.
- [41] C.-H. Ho, C.-H. Chan, Y.-S. Huang, L.-C. Tien, L.-C. Chao, The study of optical band edge property of bismuth oxide nanowires $\alpha\text{-Bi}_2\text{O}_3$, *Optic Express* 21 (2013) 11965, <https://doi.org/10.1364/oe.21.011965>.
- [42] G. Alessio Verni, B. Long, F. Gity, M. Lanusi, P. Schüfflgen, G. Mussler, D. Grützmacher, J. Greer, J.D. Holmes, Oxide removal and stabilization of bismuth thin films through chemically bound thiol layers, *RSC Adv.* 8 (2018) 33368–33373, <https://doi.org/10.1039/C8RA06840B>.
- [43] Y.C. Liang, C.C. Wang, Surface crystal feature-dependent photoactivity of ZnO-ZnS composite rods: via hydrothermal sulfidation, *RSC Adv.* 8 (2018) 5063–5070, <https://doi.org/10.1039/c7ra13061a>.
- [44] D.K. Mishra, J. Mohapatra, M.K. Sharma, R. Chattarjee, S.K. Singh, S. Varma, S.N. Behera, S.K. Nayak, P. Entel, Carbon doped ZnO : synthesis, characterization and interpretation, *J. Magn. Magn Mater.* 329 (2013) 146–152, <https://doi.org/10.1016/j.jmmm.2012.09.058>.
- [45] S. Kang, R.C. Pawar, Y. Pyo, V. Khare, C.S. Lee, Size-controlled BiOCl-RGO composites having enhanced photodegradative properties, *J. Exp. Nanosci.* 11 (2016) 259–275, <https://doi.org/10.1080/17458080.2015.1047420>.
- [46] M. Jamil, Z.S. Khan, A. Ali, N. Iqbal, Studies on solution processed Graphene- Nb_2O_5 nanocomposite based photoanode for dye-sensitized solar cells, *J. Alloys Compd.* 694 (2017) 401–407, <https://doi.org/10.1016/j.jallcom.2016.09.300>.
- [47] O.F. Lopes, E.C. Paris, C. Ribeiro, Synthesis of Nb_2O_5 nanoparticles through the oxidant peroxide method applied to organic pollutant photodegradation: a mechanistic study, *Appl. Catal. B Environ.* 144 (2014) 800–808, <https://doi.org/10.1016/j.apcatb.2013.08.031>.
- [48] Q. Wang, C. Zhang, H. Wu, Q. Gao, R. Duan, C. Chen, Fabrication of β -phase AgI and Bi_2O_3 co-decorated $\text{Bi}_2\text{O}_3\text{CO}_3$ heterojunctions with enhanced photocatalytic performance, *J. Colloid Interface Sci.* 547 (2019) 1–13, <https://doi.org/10.1016/j.jcis.2019.03.088>.
- [49] K. Elghniji, O. Hentati, N. Mlaik, A. Mahfoudh, M. Ksibi, Photocatalytic degradation of 4-chlorophenol under P-modified TiO_2/UV system: kinetics, intermediates, phytotoxicity and acute toxicity, *J. Environ. Sci.* 24 (2012) 479–487, [https://doi.org/10.1016/S1001-0742\(10\)60659-6](https://doi.org/10.1016/S1001-0742(10)60659-6).
- [50] C. Yang, Q. Li, L. Tang, K. Xin, A. Bai, Y. Yu, Synthesis, photocatalytic activity, and photogenerated hydroxyl radicals of monodisperse colloidal ZnO nanospheres, *Appl. Surf. Sci.* 357 (2015) 1928–1938, <https://doi.org/10.1016/j.apsusc.2015.09.140>.
- [51] J. Zhang, Y. Nosaka, Mechanism of the OH radical generation in photocatalysis with TiO_2 of different crystalline types, *J. Phys. Chem. C* 118 (2014) 10824–10832,

- <https://doi.org/10.1021/jp501214m>.
- [52] Y. Nosaka, A.Y. Nosaka, Generation and detection of reactive oxygen species in photocatalysis, *Chem. Rev.* 117 (2017) 11302–11336, <https://doi.org/10.1021/acs.chemrev.7b00161>.
- [53] P. She, S. Yin, Q. He, X. Zhang, K. Xu, Y. Shang, X. Men, S. Zeng, H. Sun, Z. Liu, A self-standing macroporous Au/ZnO/reduced graphene oxide foam for recyclable photocatalysis and photocurrent generation, *Electrochim. Acta* 246 (2017) 35–42, <https://doi.org/10.1016/j.electacta.2017.06.027>.
- [54] J. Lee, Z. Li, L. Zhu, S. Xie, X. Cui, Ti^{3+} self-doped TiO_2 via facile catalytic reduction over $\text{Al}(\text{acac})_3$ with enhanced photoelectrochemical and photocatalytic activities, *Appl. Catal. B Environ.* 224 (2018) 715–724, <https://doi.org/10.1016/j.apcatb.2017.10.057>.
- [55] S. Yi, X. Yue, D. Xu, Z. Liu, F. Zhao, D. Wang, Y. Lin, Study on photogenerated charge transfer properties and enhanced visible-light photocatalytic activity of p-type Bi_2O_3 /n-type ZnO heterojunctions, *New J. Chem.* 39 (2015) 2917–2924, <https://doi.org/10.1039/c4nj01738b>.